

# Temporal and spatial variability in the hydrothermal signature of sinking particles and sediments in the Western Tropical South Pacific Ocean

Chloé Tilliette<sup>1</sup>, Frédéric Gazeau<sup>1</sup>, Valerie Chavagnac<sup>2</sup>, Nathalie Leblond<sup>3</sup>, Maryline Montanes<sup>1</sup>, Karine Leblanc<sup>4</sup>, Sabine Schmidt<sup>5</sup>, Bruno Charrière<sup>6</sup>, Nagib Bhairy<sup>4</sup>, and Cécile Guieu<sup>7</sup>

<sup>1</sup>Sorbonne Université, CNRS, Laboratoire d’Océanographie de Villefranche

<sup>2</sup>Geosciences Environnement Toulouse, Université de Toulouse

<sup>3</sup>LOV-CNRS UMR 7093

<sup>4</sup>MIO, CNRS - Université Aix-Marseille

<sup>5</sup>Université de Bordeaux, EPOC, UMR 5805 CNRS

<sup>6</sup>CEFREM

<sup>7</sup>Laboratoire d’Océanographie de Villefranche, LOV

November 7, 2023

# Significant impact of hydrothermalism on the biogeochemical signature of sinking and sedimented particles in the Lau Basin

1 **Chloé Tilliette<sup>1</sup>, Frédéric Gazeau<sup>1</sup>, Valérie Chavagnac<sup>2</sup>, Nathalie Leblond<sup>1</sup>, Maryline Montanes<sup>1</sup>,**  
2 **Karine Leblanc<sup>3</sup>, Sabine Schmidt<sup>4</sup>, Bruno Charrière<sup>5</sup>, Nagib Bhairy<sup>3</sup>, Cécile Guieu<sup>1\*</sup>**

3 <sup>1</sup>Sorbonne Université, CNRS, Laboratoire d'Océanographie de Villefranche, LOV, 06230,  
4 Villefranche-sur-Mer, France

5 <sup>2</sup>Géosciences Environnement Toulouse, GET, CNRS, UPS, Université de Toulouse, IRD, Toulouse,  
6 France

7 <sup>3</sup>Aix Marseille Univ., Université de Toulon, CNRS, IRD, MIO, Marseille, France.

8 <sup>4</sup>Univ. Bordeaux, CNRS, Bordeaux INP, EPOC, UMR 5805, F-33600 Pessac, France

9 <sup>5</sup>Centre de Formation et de Recherche sur l'Environnement Méditerranéen (CEFREM, UMR CNRS  
10 5110), Bât. U, Université de Perpignan, Via Domitia (UPVD), Perpignan, France

## 11 \* Correspondence:

12 Chloé Tilliette, Cécile Guieu

13 [chloe.tilliette@imev-mer.fr](mailto:chloe.tilliette@imev-mer.fr); [cecile.guieu@imev-mer.fr](mailto:cecile.guieu@imev-mer.fr)

14 **Keywords: hydrothermal impacts, biological production, composition of sinking and**  
15 **sedimented material, trace metals, Tonga volcanic Arc, Western Tropical South Pacific Ocean**

16 Number of words: 8,286

17 Number of tables/figures: 3 tables, 7 figures

## 18 Abstract

19 Iron (Fe) is an essential micronutrient for diazotrophs, which are abundant in the Western Tropical  
20 South Pacific Ocean (WTSP). Their success depends on the numerous trace metals, particularly Fe,  
21 released from shallow hydrothermal vents along the Tonga Arc. This study aimed to explore the spatio-  
22 temporal impact of hydrothermal fluids on particulate trace metal concentrations and biological  
23 activity. To identify the composition of sinking particles across a wide area of the WTSP, we deployed  
24 sediment traps at various depths, both close and further west of the Tonga Arc. Seafloor sediments  
25 were cored at these deployment sites, including at a remote location in the South Pacific Gyre. The  
26 sinking particles were composed of a large amount of biological material (up to 88 mg d<sup>-1</sup>), indicative

27 of the high productivity of the region. A significant portion of this material ( $\sim 21 \pm 12$  wt.%) was  
28 lithogenic of hydrothermal origin, as revealed through Al-Fe-Mn tracing. The sinking material showed  
29 similar patterns between lithogenic and biogenic fractions, indicating that hydrothermal input within  
30 the photic layer triggered surface production. A hydrothermal fingerprint was suggested in the  
31 sediments due to the high sedimentation rates ( $> 47$  cm kyr<sup>-1</sup>) and the presence of large, heterogeneous,  
32 metal-rich particles. The presence of nearby active deep hydrothermal sources was suspected near the  
33 Lau Ridge due to the large particle size (1-976  $\mu$ m) and the significant excess of Fe and Mn (2-20  
34 wt.%). Overall, this study revealed that hydrothermal sources have a significant influence on the  
35 biogeochemical signature of particles in the region.

### 36 **Plain Language Summary**

37 Iron is an essential micronutrient for phytoplankton growth, especially diazotrophs. In a certain area of  
38 the Pacific Ocean, they can obtain the iron they need from material released by hydrothermal vents  
39 along the Tonga Arc. We demonstrated how hydrothermal sources affect the amount of iron and other  
40 materials released into the water column and their influence on phytoplankton. We collected sinking  
41 particles and seafloor sediments and examined their chemical composition. The sinking material  
42 consisted of a large amount of biological material, indicative of the high productivity of the area. A  
43 large part of the particles collected were minerals from hydrothermal vents. These biological and  
44 metallic materials displayed similar export patterns, indicating the role of hydrothermal sources in  
45 driving surface ocean productivity. Seafloor sediments were also influenced by hydrothermalism, as  
46 suggested by their high metal contents, high sedimentation rates and large, heterogeneous particle size.  
47 In addition, an undiscovered hydrothermal source was potentially identified near the Lau Ridge based  
48 on these data. Overall, this study revealed the significant impact of hydrothermalism on the  
49 biogeochemical signature of the particles in the Lau Basin at large spatial and temporal scales.

## 50 **1 Introduction**

51 The Western Tropical South Pacific (WTSP) Ocean (160 °E to 160 °W) has been identified as a hotspot  
52 for dinitrogen (N<sub>2</sub>) fixation by diazotroph organisms (Bonnet et al., 2017). The success of these species  
53 relies on the high, non-limiting surface concentrations (> 0.3 nmol L<sup>-1</sup>; Johnson et al., 1997) of iron  
54 (Fe) in the region, as Fe is a major component of the nitrogenase enzyme that catalyzes the N<sub>2</sub> fixation  
55 process (Raven, 1988). Recently, Tilliette et al. (2022) revealed that these high dissolved Fe (DFe)  
56 concentrations (up to 48 nmol L<sup>-1</sup>) originate from shallow hydrothermal sources (< 300 m) hosted along  
57 the Tonga-Kermadec Arc that fertilize the photic zone of the entire Lau Basin with DFe, forming a  
58 productivity patch as large as 360,000 km<sup>2</sup> (analogous to the Caspian Sea area; Bonnet, Guieu et al.,  
59 2023).

60 The Tonga-Kermadec Arc is the most linear, convergent and seismically active subduction zone on  
61 Earth (Timm et al., 2013) and consequently exhibits the highest density of submarine volcanoes and  
62 associated hydrothermal sources (Massoth et al., 2007; Pelletier et al., 1998; Stoffers et al., 2006). Such  
63 systems release extensive plumes enriched in numerous chemical species relative to the overlying  
64 water column (Dick et al., 2013; González-Vega et al., 2020; Lilley et al., 2013) including gases (e.g.,  
65 H<sub>2</sub>S – hydrogen sulfide, CO<sub>2</sub> – carbon dioxide, CH<sub>4</sub> – methane), macronutrients and dissolved and  
66 particulate trace metals (e.g., Fe, Mn – manganese, Cu – copper, Zn – zinc, Pb – lead, Ni – nickel). In  
67 the Lau Basin, most of these plumes originate from sources located at depth (> 1000 m; Beaulieu and  
68 Szafranski, 2020; Lupton et al., 2004; Massoth et al., 2007), but shallower active sources (< 500 m)  
69 have also been identified (Beaulieu and Szafranski, 2020; Guieu et al., 2018; Massoth et al., 2007).  
70 Two shallow hydrothermal sites were investigated as part of the TONGA cruise (Guieu and Bonnet,  
71 2019), revealing an 80-fold enrichment of DFe concentrations (< 0.45 μm) above the source relative  
72 to unimpacted waters of the WTSP (Tilliette et al., 2022). Despite their decrease towards the surface,  
73 elevated concentrations (0.6-10 nmol L<sup>-1</sup>) persisted in the photic layer (0-150 m) allowing to sustain

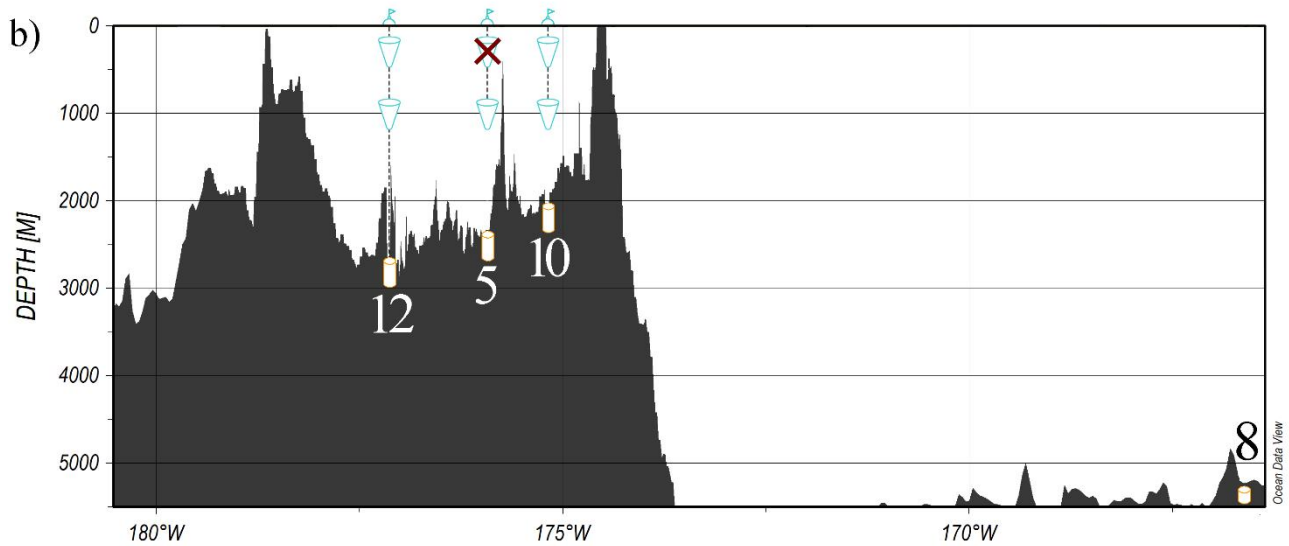
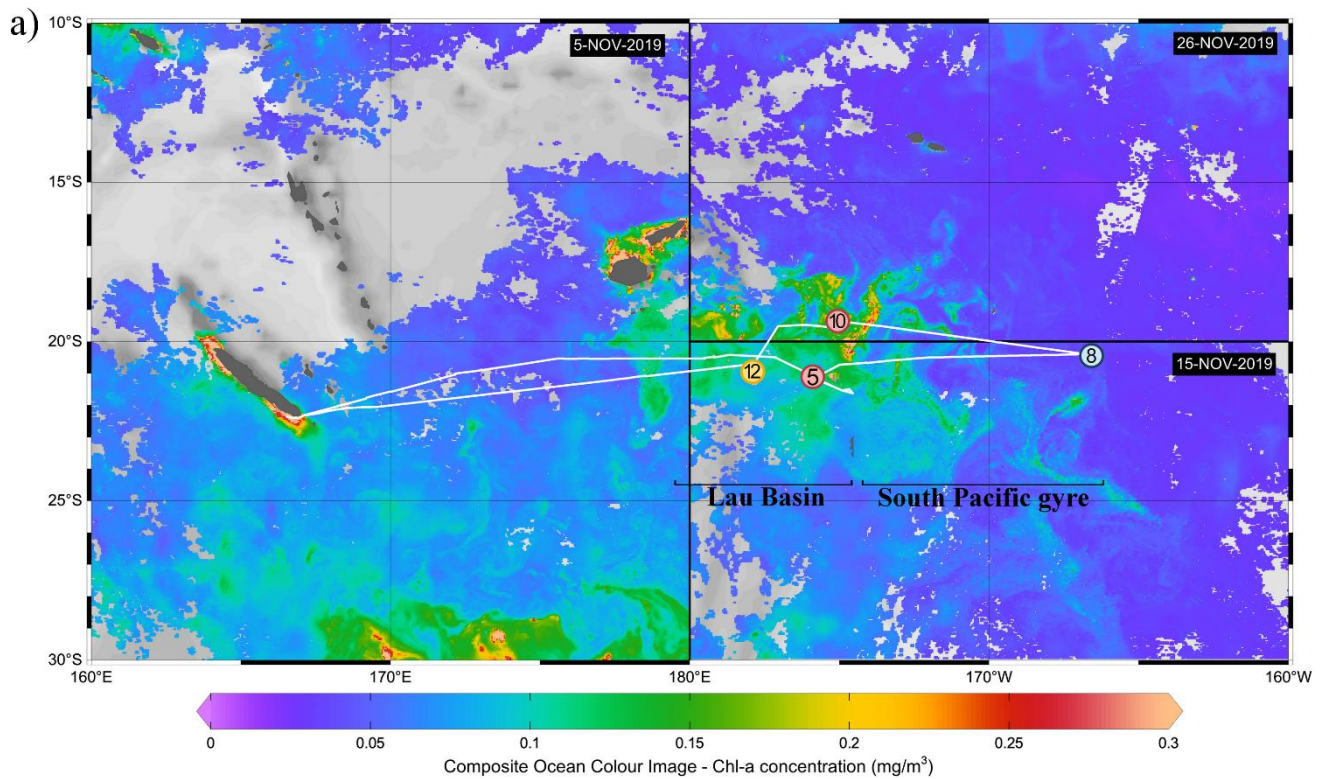
74 high rates of primary production (90-145 mmol C m<sup>-2</sup> d<sup>-1</sup>). Although the effects of such hydrothermal  
75 fertilization on biological activity are beginning to be elucidated on short temporal scales (Tilliette et  
76 al., 2023), its effects on the biogeochemical signature of the exported and sedimented particles on  
77 larger temporal and spatial scales remain unclear.

78 Sediment traps are classically used to explore biogeochemical cycles in the ocean and since pioneering  
79 studies (e.g., Deuser, 1987; Deuser and Ross, 1980; Honjo et al., 1992), these devices have shown their  
80 potential to highlight the variability of the composition and fluxes of biological material in relation to  
81 surface productivity, depth or season. On their descent, in particular in the mesopelagic zone (200-  
82 1000 m), biological particles are subjected to intense bacterial remineralization and grazing by  
83 zooplankton (Boyd and Trull, 2007; Ducklow et al., 2001; Volk and Hoffert, 2013). Only a minor  
84 proportion of this material will eventually reach the deep-sea (> 1000 m) and an even smaller  
85 proportion will be buried in seafloor sediments (Berger et al., 1989; Hüneke and Henrich, 2011).

86 In this study, we determined the composition (i.e., lithogenic, organic matter, calcium carbonate –  
87 CaCO<sub>3</sub> and opal) of sinking and sedimented particles at different spatial and temporal scales over a  
88 large area of the WTSP, including two sites located along the Tonga Arc. The aim was to better  
89 understand how hydrothermal activity influences this region, both in terms of hydrothermally-derived  
90 trace metal concentrations and their influence on biological activity, and how volcanic activity impacts  
91 the footprint of metal particles. Ultimately, this study established whether hydrothermal sources have  
92 a significant influence on the biogeochemical signature of particles in the Lau Basin at large spatial  
93 (up to 200 km from the arc, over the entire water column) and temporal (from seasonal to centennial  
94 scales in seafloor sediments) scales.

## 95 **2 Material and methods**

96 This study was conducted as part of the TONGA cruise (GEOTRACES GPpr14; Guieu and Bonnet,  
97 2019) onboard the R/V L'Atalante from October 31 to December 5, 2019, along a 6100 km-long  
98 transect crossing the Lau Basin (*Fig. 1*). Two shallow hydrothermal sources were identified at depths  
99 of 200 and 300 m, respectively (Tilliette et al., 2022). Mooring lines were deployed west of these  
100 sources (~15 km; stations 5 and 10) along the main current direction once the seafloor reached ~2000  
101 m.



102

103 **Figure 1. (a)** Cruise transect superimposed on surface chlorophyll-*a* concentrations ( $\text{mg m}^{-3}$ ; Bonnet, Guieu et al.,  
 104 2023). Different oceanic regions were occupied during the cruise: the South Pacific gyre (station 8; sediment coring  
 105 only) and the Lau Basin (stations 5 and 10), where a drifting mooring line was deployed for 5 and 4 days, respectively,  
 106 as well as station 12 where a fixed mooring line was deployed for one year. Sediments were cored at each of these  
 107 stations. Chlorophyll-*a* concentrations were derived from satellite images acquired during the respective period of  
 108 occupancy: 5 November 2019 for the western part of the transect, 15 November for the southeastern part, and 29  
 109 November for the northeastern part. **(b)** Bathymetry along the cruise transect and instrumentation deployed at each  
 110 station: sediment traps (cones) and sediment coring (cylinders).

## 111 2.1 Fieldwork

112 At stations 5 and 10, drifting conical sediment traps with a collection area of 1 m<sup>2</sup> (PPS-5, Technicap,  
113 France) were deployed at 200 and 1000 m on a surface-tethered drifter. Settling particles were collected  
114 at 24-h intervals for 5 days at station 5 (21°9.14' S, 175°44.42' W; November 10-14, 2019), and at 23-  
115 h intervals for 4 days at station 10 (19°24.54' S, 175°7.34' W; November 24-27, 2019). Unfortunately,  
116 due to a malfunction of the PPS-5 plate motor, no samples were collected at 200 m at station 5. At  
117 station 12 (20°42.41' S, 177°52.13' W), two PPS-5 were deployed at 200 and 1000 m on a fixed  
118 mooring line for one year (November 2019 to October 2020, sampling interval: 14 days). The fixed  
119 mooring line was equipped with two inclinometers (NKE S2IP) and two current meters (Nortek  
120 Aquadopp) placed at 222 and 1030 m. The angles and velocities at both depths are shown in *Fig. S1*.  
121 Each collection cup was filled with a 5% buffered formaldehyde solution prepared with filtered *in-situ*  
122 seawater to prevent microbial degradation and swimmer grazing. After trap recovery during the  
123 TONGA-RECUP cruise onboard the R/V Alis in December 2020 (Guieu, 2020), the cups were stored  
124 in the dark at 4 °C.

125 Sediment cores were collected at around 10 p.m. using a MC-8/100 multi-corer (Oktopus GmbH, Kiel,  
126 Germany) at the mooring positions and at the deep-sea reference site (station 8; 20°23.33' S, 166°25.4'  
127 W; *Fig. 1*). The seafloor depth for each core is specified in *Table 1*. Immediately after collection, the  
128 first 16 cm of collected cores were divided into 1 to 5 cm slices, depending on the stations (see *Fig. 3*)  
129 and frozen at -20 °C.

130 **Table 1.** Composition (wt.% – percentage by weight) and sedimentation rate of seafloor sediments at each station.

Station	Depth	CaCO <sub>3</sub>	Opal	Organic matter	Lithogenic	Sedimentation rates
-	<i>m</i>			<i>wt. %</i>		<i>cm kyr<sup>-1</sup></i>
Station 5	2140	2 ± 1	9 ± 1	0.1 ± 0.03	90 ± 1	58 ± 10
Station 10	1930	4 ± 1	7 ± 1	0.1 ± 0.03	88 ± 3	47 ± 7
Station 12	1940	64 ± 1	13 ± 1	0.4 ± 0.1	23 ± 3	61 ± 6
Station 8	5326	0.3 ± 0.1	11 ± 0.1	0.6 ± 0.2	88 ± 2	58*

131 *Note.* Due to Ra enrichment of probable hydrothermal origin at station 8, the estimated sedimentation rate has been  
132 given as an indication only (see section 3.4).

## 133 **2.2 Laboratory work**

### 134 *2.2.1 Elemental composition of sinking material and seafloor sediments*

135 Sediment trap samples were processed by the “Cellule Pièges” (INSU-CNRS: [https://www.imev-](https://www.imev-mer.fr/web/?p=526)  
136 [mer.fr/web/?p=526](https://www.imev-mer.fr/web/?p=526)). For each sediment trap cup, swimmers were carefully removed with Teflon  
137 tweezers under a stereomicroscope (Leica Wild MZ8). Any visible material attached to the swimmers  
138 was removed whenever possible, to avoid biasing particle flux. Samples were then rinsed three times  
139 with 50 mL of MilliQ water to remove salts and lyophilized for seven days. The total weight (wt) of  
140 each sample was measured on a Sartorius precision balance ( $\pm 0.01$  mg).

141 Seafloor sediment samples were thawed at room temperature and lyophilized for seven days.

142 Both seafloor sediments and sediment trap samples were then split in different pre-weighted aliquots  
143 (~10-20 mg) for various analyses. Total carbon was measured with a CHN elemental analyzer (2400  
144 Series II CHNS/O, Perkin Elmer®; precision  $\pm 0.3\%$ ). Particulate organic carbon (POC) was  
145 determined similarly, after particulate inorganic carbon (PIC) removal by acidification with 2 N  
146 hydrochloric acid. Biogenic (BSi) and lithogenic (LSi) silica measurements were performed after  
147 sodium hydroxide (NaOH) and hydrofluoric acid (HF) digestion following the exact protocol described  
148 by Mosseri et al. (2005) and adapted from Brzezinski and Nelson (1995). For each aliquot, BSi was  
149 initially dissolved by NaOH digestion at 95 °C for 5 h. LSi was then extracted from the same aliquot  
150 by HF digestion at room temperature for 48 h. For both digests, the dissolved silicic acid (DSi)

151 concentrations of the resulting solutions were analyzed according to Nelson et al. (1989) with a UV-  
152 Vis spectrophotometer (Analytikjena® Spector 250 plus). DSi concentrations were also measured in  
153 the supernatant of each trap cup to account for BSi dissolution during trap deployment and were added  
154 to the BSi value determined by digestion (Hurd, 1972; Nelson et al., 1995; Nelson and Brzezinski,  
155 1997). Several aliquots of certified reference material (GBW: marine sediment, NRCC) were digested  
156 and analyzed under the same conditions, allowing validation of Si data. GBW standard analyses  
157 averaged  $28.5 \pm 0.5$  wt.% total Si (BSi + LSi ;  $n = 12$ ), which compares well with the community  
158 consensus concentrations of  $25.2 \pm 0.6$  wt.%. Al, Ca, Cu, Fe, Mn, Ni, Pb, Si and Zn concentrations  
159 were measured by ICP-OES (Inductively-Coupled Plasma Optical Emission Spectrometry; Perkin-  
160 Elmer® Optima-8000) after acid digestion of ~20 mg particulate aliquots in Teflon vials by successive  
161 addition of (1) 1 mL of 65% nitric acid ( $\text{HNO}_3^-$ ) followed by (2) 500  $\mu\text{L}$  of 65%  $\text{HNO}_3^-$  and 500  $\mu\text{L}$   
162 HF. At each step, aliquots were heated at 150 °C for 5 h. Several reagent blanks and certified reference  
163 material (GBW) were digested and analyzed under the same conditions. Blanks were below or close  
164 to the detection limits of the instrument and the percentage recovery obtained for the certified materials  
165 indicated accurate digestion and quantitative analysis for all elements (*Table S1*).

166 Dry material collected in acrylic traps deployed at 1000 m on the drifting mooring line at Station 10  
167 was filtered onto 0.2  $\mu\text{m}$  polycarbonate filters, rinsed with distilled water and dried at room  
168 temperature. Filters were then coated with gold and observed using a Phenom scanning electron  
169 microscope at 10 kV.

### 170 2.2.2 Grain size distribution of seafloor sediments

171 Grain size of sediments was determined at the Centre de Formation et de Recherche sur les  
172 Environnements Méditerranéens (CEFREM; France) laboratory using a Malvern Mastersize 3000 laser  
173 granulometer (precision  $\pm 3\%$ ). Prior to measurement, dry sediments were homogenized, diluted in  
174 distilled water in order to achieve the concentration required by the software (i.e., 5-20% obscuration)

175 and ultrasonicated for 5 minutes. Since the number distribution may underestimate the larger particles,  
176 a particle size distribution based on a spherical equivalent volume model was used. The size of a  
177 particle was then represented by the diameter of an equivalent sphere of equal volume.

### 178 2.2.3 Sedimentation rates of seafloor sediments

179 Sedimentation rates were determined using  $^{210}\text{Pb}$ , a natural decay-product of  $^{226}\text{Ra}$  with a half-life of  
180 22.3 years.  $^{210}\text{Pb}$  deposited at the seabed by sedimentation is referred to as  $^{210}\text{Pb}$  in excess ( $^{210}\text{Pb}_{\text{XS}}$ )  
181 relative to that found within sediment. Considering constant flux and accumulation rate (Robbins and  
182 Edgington, 1975), sedimentation rates were derived from the decrease of  $^{210}\text{Pb}_{\text{XS}}$  activities with depth  
183 according to the following formula:

$$184 \quad [^{210}\text{Pb}_{\text{XS}}]_z = [^{210}\text{Pb}_{\text{XS}}]_0 * e^{\left(-\frac{\lambda}{\text{SAR}}z\right)} \quad (1)$$

185 with  $[^{210}\text{Pb}_{\text{XS}}]_0$  and  $[^{210}\text{Pb}_{\text{XS}}]_z$ ; the excess  $^{210}\text{Pb}$  activities at the water-sediment interface and at depth  
186  $z$ , respectively;  $\lambda$ , the nuclide decay constant and SAR, the sediment accumulation rate. The activities  
187 of  $^{210}\text{Pb}$  and  $^{226}\text{Ra}$  were determined at the Environnements et Paléoenvironnements Océaniques et  
188 Continentaux (EPOC; France) laboratory on dry sediments using a low background, high efficiency  
189 well-type gamma spectrometer (CANBERRA; Schmidt et al., 2014).

### 190 2.3 Composition of the exported particles and sediments

191 The elemental analyses described above were used to determine the four main fractions of the collected  
192 sinking and sedimented material: organic matter (OM), calcium carbonates ( $\text{CaCO}_3$ ), opal and  
193 lithogenic. The OM fraction was calculated from POC concentrations as  $2.199 \times \text{POC}$  (Klaas and  
194 Archer, 2002). The  $\text{CaCO}_3$  fraction was estimated from PIC as  $\text{CaCO}_3 = \text{PIC} \times 8.33$  (Verardo et al.,  
195 1990). PIC was preferentially used, as the method from Ca tended to overestimate the  $\text{CaCO}_3$  fraction  
196 on some samples ( $> 100$  wt.% of total collection weight; *Table S2*), likely due to the presence of

197 lithogenic Ca. The opal fraction was determined from BSi concentrations as  $Opal = BSi \times 2.4$   
198 (Mortlock and Froelich, 1989). Finally, the lithogenic fraction was determined through the mass  
199 balance method (Wefer and Fischer, 1993), by subtracting the sum of the above three fractions from  
200 the total collection weight. This method was preferentially chosen in view of the potential bias of using  
201 lithogenic tracers (LSi or Al) in this region, as these two elements can be significantly enriched or  
202 depleted through volcanic or hydrothermal activity, as discussed in section 4.3.

## 203 **2.4 Trace metal in sinking particles and seafloor sediments**

204 *Calcium carbonate-free basis.* The bulk metal concentration was corrected for biogenic calcium  
205 carbonate concentration, following the approach described by German et al. (1997). Indeed, as  $CaCO_3$   
206 contains very low levels of trace elements, it can dilute the metal contribution of the collected material.  
207 Prior to any interpretation, the concentration of an element (E) was corrected on a calcium carbonate-  
208 free basis (*cfb*) following:

$$209 \quad [E]_{cfb} = \frac{[E]}{(100 - \%CaCO_3)} \quad (2)$$

210 *Metal content.*  $[E]_{cfb}$  of sinking and sedimented material was compared to the concentrations of  
211 reference pelagic clays sampled in the Pacific Ocean (“pc”; *Table 2*; Li and Schoonmaker, 2003; Sayles  
212 and Bischoff, 1973) using two distinct methods: enrichments factors (EF) and metal excess (XS).

### 213 **2.4.1 Enrichment factors in sinking particles**

214 For the sinking material, EF were calculated by normalizing the concentration ratio of an element ( $E$ )<sub>cfb</sub>  
215 to aluminum ( $Al$ )<sub>cfb</sub>, lithogenic tracer) to the same elemental ratio measured in pelagic clays following  
216 the formula:

$$217 \quad E_{EF} = \frac{[E]_{cfb \text{ sample}}/[Al]_{cfb \text{ sample}}}{[E]_{pc}/[Al]_{pc}} \quad (3)$$

218 **Table 2.** Elemental enrichment factors ( $E_{EF}$ ) of metals in sinking material relative to aluminum ( $Al_{cfb}$ ) and average  
 219 concentrations in reference pelagic clays.

Sample	Fe	Mn	Cu	Zn	Ni	LSi
Station 5 - 1000 m	<b>1.4</b>	<i>0.2</i>	<i>0.6</i>	<b>11</b>	1.1	<b>5.2</b>
Station 10 - 200 m	1.1	<b>5.0</b>	<b>18</b>	<b>37</b>	<b>7.3</b>	<i>0.4</i>
Station 10 - 1000 m	1.0	<i>0.01</i>	<i>0.03</i>	<i>0.7</i>	<i>0.1</i>	<b>14</b>
Station 12 - 200 m	1.1	<i>0.02</i>	<i>0.2</i>	<b>6.1</b>	<i>0.1</i>	<i>0.2</i>
Station 12 - 1000 m	<b>1.7</b>	<i>0.6</i>	<b>2.0</b>	<b>39</b>	<b>2.7</b>	<b>1.6</b>
Reference pelagic clays	$5.9 \pm 0.6$	$1.1 \pm 0.4$	$469 \pm 181$	$158 \pm 12$	$196 \pm 14$	$25 \pm 1$

220 *Note.* Enrichments relative to Pacific Ocean pelagic clays ( $EF > 1$ ) are shown in bold while depletions relative to the  
 221 reference ( $EF < 1$ ) are shown in italics. Average concentrations and standard deviations (in wt.% for Fe, Mn and LSi  
 222 and ppm for Cu, Zn and Ni) within several reference pelagic clays (from Li and Schoonmaker, 2003; Sayles and  
 223 Bischoff, 1973; Taylor and McLennan, 1985) are shown at the bottom of the table. Note that the range of  
 224 concentrations measured for each element in these references provides only a rough estimate of metal non-detrital  
 225 enrichment in the material collected in this study. It may therefore over- or underestimate the magnitude of these  
 226 enrichments.

#### 227 **2.4.2 Elemental excess in seafloor sediments**

228 For seafloor sediments, metal excess relative to reference pelagic clay composition was determined by  
 229 correcting  $[E]_{cfb}$  for detrital inputs (German et al., 1997) assuming that this reference material was  
 230 representative of a deep-sea detrital end-member. Detrital concentrations of each element were  
 231 calculated according to:

$$232 \quad [E]_{det} = [Al]_{cfb} * \frac{[E]_{pc}}{[Al]_{pc}} \quad (4)$$

233 It is important to note that this calculation assumes that all sedimentary Al originates from detrital  
 234 material. However, sedimentary Al concentrations could originate from both hydrothermal and detrital  
 235 sources (Massoth et al., 1998; Resing and Sansone, 1999; Von Damm, 1990). Consequently, Al  
 236 normalization may have underestimated the extent of hydrothermal enrichment in our seafloor  
 237 sediments (Chavagnac et al., 2008). That fraction of non-detrital origin, denoted  $[E]_{XS}$ , was determined  
 238 by subtracting  $[E]_{det}$  from  $[E]_{cfb}$ , as follows:

$$239 \quad [E]_{XS} = [E]_{cfb} - [E]_{det} \quad (5)$$

## 240 **2.5 Statistical analysis**

241 To determine if significant differences could be observed in the fractions of material collected at the  
242 different stations, a non-parametric Mann-Whitney test was performed. This two-tailed distribution-  
243 free test was selected due to the non-normally distributed data, previously determined through a  
244 Kolmogorov-Smirnov test. Differences were considered significant at a p-value ( $p$ ) < 0.05.

## 245 **3 Results**

### 246 **3.1 Composition of the sinking particles and seafloor sediments**

#### 247 *3.1.1 Biogenic particles*

248 Three fractions of the collected material can be used as proxies for biological production: CaCO<sub>3</sub>, opal  
249 and OM. It should be noted that due to the strong seasonal effect prevalent in the region (see *Figs. 2e-*  
250 *h*), the quantities of biological material collected in the drifting traps (4-5 days during the austral  
251 summer) will only be compared to the quantities of the same material collected in the fixed trap during  
252 the austral summer period (i.e., from December 2019 to April 2020), and not over the whole year.

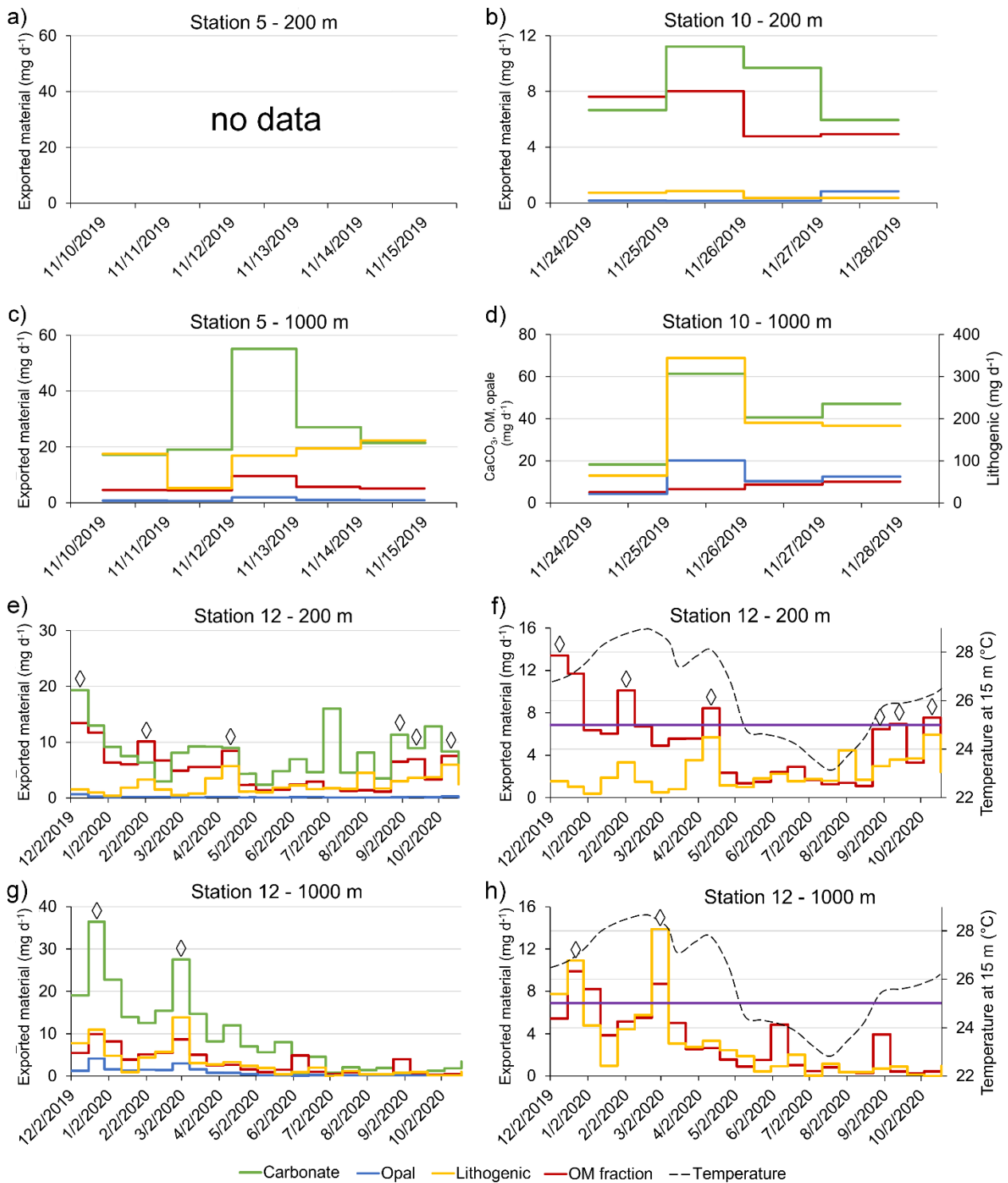
253 *Exported particles.* CaCO<sub>3</sub> was the most abundant biogenic component of the exported material during  
254 the austral summer (on average over stations and depths: 48-59 wt.%; *Fig. S2*) if station 10 at 1000 m  
255 is excluded (average 17 wt.%). The amount of CaCO<sub>3</sub> collected during the austral summer averaged  
256  $18 \pm 10 \text{ mg d}^{-1}$  at all stations and depths, with a significantly higher accumulation at 1000 m ( $\sim 25 \pm 12$   
257  $\text{mg d}^{-1}$ ;  $p < 0.05$ ; *Fig. 2*) than at 200 m ( $\sim 9 \pm 3 \text{ mg d}^{-1}$ ). In comparison, quantities collected during the  
258 austral winter at station 12 (fixed mooring) were much lower ( $\sim 5 \pm 3 \text{ mg d}^{-1}$ ), particularly at 1000 m  
259 ( $p < 0.05$ ). At this station, only two CaCO<sub>3</sub> peaks were observed at 1000 m (in December and February)  
260 while they were more frequent at 200 m. Opal fraction was the smallest biogenic component of the  
261 sinking material during the austral summer (1-5 wt.%; *Fig. S2*), regardless of station and collection  
262 depth ( $\sim 2.1 \pm 2.4 \text{ mg d}^{-1}$ ; *Fig. 2*), with a significantly higher quantity collected at 1000 m than at 200  
263 m ( $p < 0.05$ ). In comparison, opal quantities collected during the austral winter were lower ( $\sim 0.12 \pm$

264 0.05 mg d<sup>-1</sup>) although similar at both collection depths ( $p > 0.4$ ). Two opal peaks, matching the CaCO<sub>3</sub>  
265 peaks in December and February, were observed at 1000 m at the fixed mooring station. OM fraction  
266 was the second most abundant biogenic component at 200 m during the austral summer (40-41 wt.%;  
267 *Fig. S2*), with similar amounts of material collected at all stations and depths ( $\sim 6.4 \pm 2.2$  mg d<sup>-1</sup>,  $p >$   
268 0.09, *Fig. 2*). However, these quantities decreased significantly during the austral winter at both  
269 deployment depths ( $p < 0.05$ ). At station 12, OM peaks were observed from October to May and from  
270 December to February in the traps deployed at 200 and 1000 m, respectively. At 1000 m on the same  
271 site, those peaks matched those of opal and CaCO<sub>3</sub> (*Fig. 2g*).

272 *Seafloor sediments.* The proportion of CaCO<sub>3</sub> in seafloor sediments was very low (< 5 wt.%) at most  
273 stations, except at station 12 ( $64 \pm 1$  wt.%,  $p < 0.05$ , *Table 1*). Although present in low proportions (10  
274  $\pm 2$  wt.%), opal was the most abundant biogenic component in seafloor sediments, with no difference  
275 between stations ( $p > 0.05$ ). OM proportion was less than 1 wt.% for all stations and did not differ  
276 between stations ( $p > 0.05$ ).

### 277 3.1.2 Lithogenic material

278 *Exported particles.* The smallest amount of lithogenic material was collected at 200 m at station 10  
279 ( $\sim 0.5 \pm 0.2$  mg d<sup>-1</sup>;  $3 \pm 1$  wt.%; *Figs. 2 and S2*). In contrast, at the same station at 1000 m, the lithogenic  
280 material was up to four orders of magnitude higher (maximum of 344 mg d<sup>-1</sup>;  $75 \pm 3$  wt.%). Large  
281 amounts were also collected at 1000 m at station 5 ( $\sim 16 \pm 4$  mg d<sup>-1</sup>;  $33 \pm 11$  wt.%), albeit significantly  
282 lower (by a factor of 20,  $p = 0.03$ ). In comparison, at station 12 (fixed mooring), lithogenic amounts  
283 were lower throughout the year ( $p < 0.02$ ) and of the same order of magnitude in both traps (on average  
284 for the two traps deployed at station 12:  $\sim 2.6 \pm 1.9$  mg d<sup>-1</sup>;  $\sim 16 \pm 7$  wt.%;  $p = 0.2$ ). At 200 m at station  
285 12, the observed lithogenic peaks coincided with the majority of OM peaks, except between May and  
286 September. Notably, two lithogenic peaks (up to 14 mg d<sup>-1</sup>), matching those of all biogenic components  
287 (CaCO<sub>3</sub>, opal, OM), were observed in December and February at 1000 m.



288

289 **Figure 2.** Temporal dynamics of exported material (mg d<sup>-1</sup>) in drifting (a-d) and fixed (e-h) sediment traps: organic  
 290 matter (red line), calcium carbonate (green line), opal (blue line) and lithogenic fraction (yellow line). Shown on the  
 291 different panels are: station 5 at 200 and 1000 m (a, c), station 10 at 200 and 1000 m (b, d) and station 12 at 200 and  
 292 1000 m (e, g). Note that the lithogenic fraction is represented on a different y-label for station 10 – 1000 m (c). Panels  
 293 (f) and (h): organic and lithogenic material (left y-label) versus temperature at 15 m (right y-label; grey dotted line)  
 294 for both traps at station 12. The diamond on panels (e-h) indicates that the peaks of at least two fractions (CaCO<sub>3</sub>,

295 lithogenic, OM, opal) overlapped on this sampling date. The purple line delineates a temperature of 25 °C.  
296 Temperature data were extracted from the World Ocean Atlas database (Locarnini et al., 2018): average monthly  
297 temperature over the period from 2005 to 2017 at 15 m, near station 12. Note that no significant annual variation in  
298 temperature was observed (12-year monthly standard deviation ranging from 0.16 to 0.67°C). Cumulative histograms  
299 of these fractions are shown in *Fig. S2*.

300 *Seafloor sediments*. The lithogenic fraction was the most abundant fraction in the seafloor sediments  
301 at stations 5, 8 and 10 (88-90 wt.%, *Table 1*). In contrast, at station 12, the lithogenic fraction was only  
302  $23 \pm 3$  wt.% ( $p < 0.001$ ), due to the dilution effect by the high CaCO<sub>3</sub> fraction.

### 303 **3.2 Trace metal content and enrichment factors**

304 Metals in sinking particles and in seafloor sediments are presented in *Figs. S3* and *S4*.

305 *EF in exported material*. Enrichment of Zn ( $Z_{\text{NEF}}$ ) was detected in the material collected from all  
306 sediment traps compared to reference pelagic clays (x6-39; *Table 2*), except at 1000 m at station 10.  
307 Slightly elevated  $\text{Fe}_{\text{EF}}$  was estimated at 1000 m at stations 5 and 12 (x1.5-1.8). No  $\text{Mn}_{\text{EF}}$  was detected  
308 in traps, except at 200 m at station 10 (x7). Significant  $\text{Ni}_{\text{EF}}$  (x3-7) were observed at 1000 m at station  
309 12 and at 200 m at station 10.  $\text{Cu}_{\text{EF}}$  was measured only in the material collected at station 10 at 200 m  
310 and station 12 at 1000 m (x18 and x2, respectively).  $\text{LSi}_{\text{EF}}$  was estimated at 1000 m at all stations, up  
311 to a factor of 14 (station 10).

312 *Elemental excess in seafloor sediments*. Several metals were in excess in the sampled sediments  
313 relative to the composition of reference pelagic clays of the Pacific (*Fig. 3*). At all depths, sediments  
314 showed marked  $\text{Fe}_{\text{XS}}$ , although significantly lower at station 8 (on average ~3 wt.%  $\text{Fe}_{\text{XS}}$ ,  $p < 0.05$ )  
315 than at stations located in the Lau Basin (up to ~5 wt.%  $\text{Fe}_{\text{XS}}$ ). Significant  $\text{Mn}_{\text{XS}}$  (~2-20 wt.%) and  
316  $\text{Cu}_{\text{XS}}$  (~100-230 ppm) were detected in all sediments, with the highest excess measured at station 12  
317 ( $p < 0.05$ ). This station also had the unique characteristic of displaying  $\text{Ni}_{\text{XS}}$  (~100 ppm),  $\text{Zn}_{\text{XS}}$  (~10  
318 ppm) and  $\text{Pb}_{\text{XS}}$  (~20 ppm) while no excess was detected at the other stations (excluding small

319 occasional Pb<sub>XS</sub> within the station 8 profile; up to 10 ppm). High LSi<sub>XS</sub> were measured at stations 5  
320 (~5 wt.%) and 10 (up to ~7 wt.%).

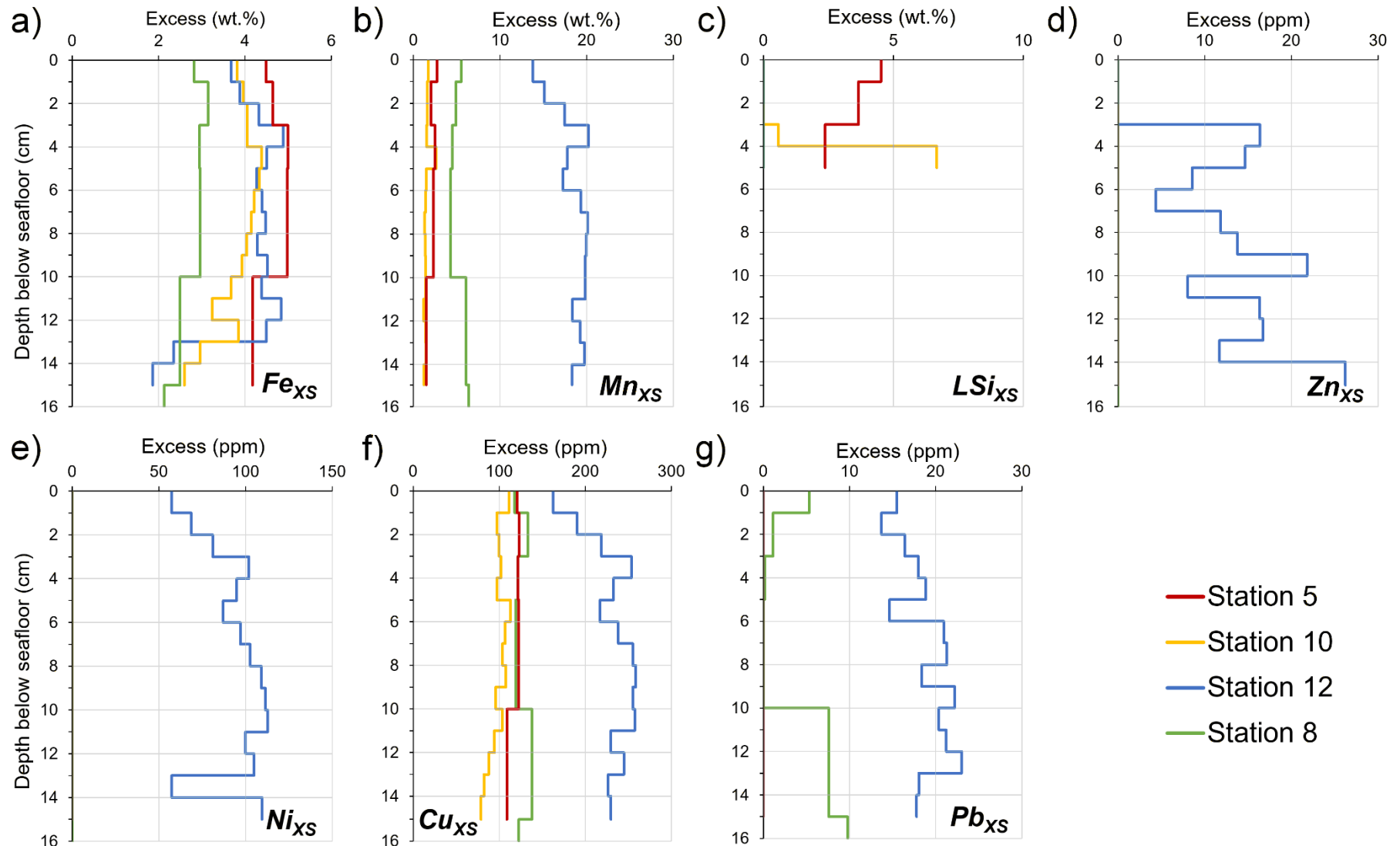


**Figure 3.** Excess of metal ( $E_{XS}$ ) in each slice of seafloor sediments relative to the composition of reference pelagic clays: (a) iron ( $Fe_{XS}$ ), (b) manganese ( $Mn_{XS}$ ),

324 (c) lithogenic silica ( $LSi_{XS}$ ), (d) zinc ( $Zn_{XS}$ ), (e) nickel ( $Ni_{XS}$ ), (f) copper ( $Cu_{XS}$ ) and (g) lead ( $Pb_{XS}$ ). Excess in major elements are represented in wt.% (Fe, Mn,  
325 Si, Ca) and minor elements (Zn, Ni, Cu, Pb) in ppm.

326 **3.3 Grain size distribution of seafloor sediments**

327 The smallest particle sizes, mainly between 2 and 16  $\mu\text{m}$ , were measured at station 8 (*Fig. 4*). Larger  
328 particles were identified at stations 5 and 10, primarily between 30 and 110  $\mu\text{m}$ . A wide range of  
329 particle sizes was measured at station 12, mainly ranging from 1 to 310  $\mu\text{m}$  and up to 976  $\mu\text{m}$ .

330

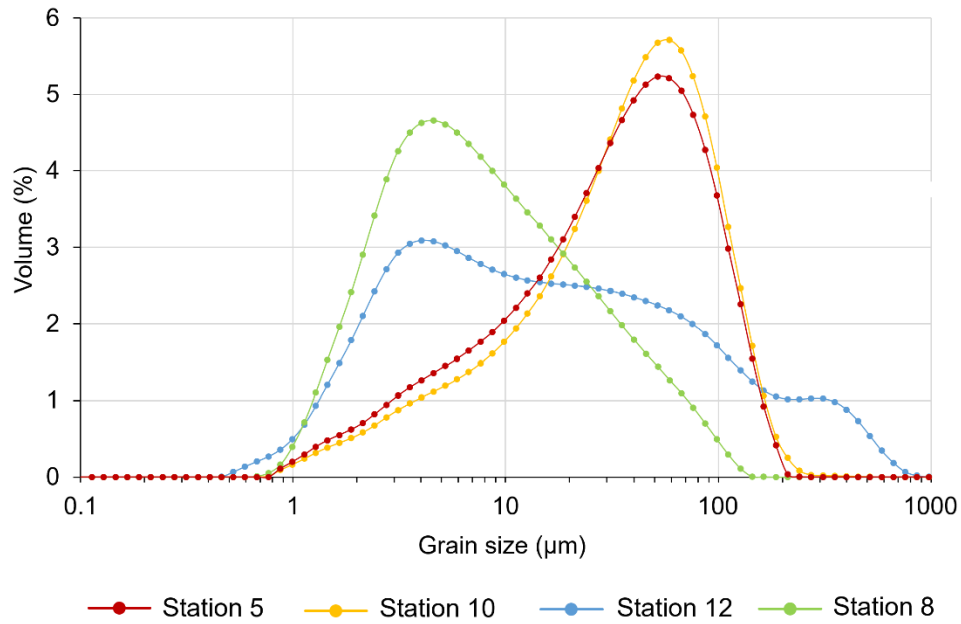


*Figure 4.* Grain size distribution averaged for all sediment slices at each station. The distribution for each sediment slice is shown in *Figure S5*.

334 **3.4 Sedimentation rate of seafloor sediments**

335  $^{210}\text{Pb}$  and  $^{210}\text{Pb}_{\text{XS}}$  activities ranged from 11 to 290  $\text{mBq g}^{-1}$  and from 1 to 259  $\text{mBq g}^{-1}$ , respectively  
336 (*Fig. S6*). Values of  $^{210}\text{Pb}_{\text{XS}}$  decreased exponentially with depth in the sediments cored at stations 5,  
337 10 and 12, reaching negligible levels at about 6 to 10 cm, depending on the core considered. This was  
338 not the case for the core from station 8, which still exhibited high  $^{210}\text{Pb}_{\text{XS}}$  in the 10-15 cm sediment  
339 layer, associated with the highest  $^{226}\text{Ra}$  values measured in the studied cores (100-200  $\text{mBq}^{-1}$ ). Such  
340 high  $^{226}\text{Ra}$  activities may be related to hydrothermal enrichment. Indeed, it could be suspected that  
341 below 3-5 cm, total  $^{210}\text{Pb}$  activities correspond to a combination of  $^{210}\text{Pb}_{\text{XS}}$  and  $^{210}\text{Pb}$  ingrowth from  
342 Ra enrichment: the deepest  $^{210}\text{Pb}_{\text{XS}}$  activities are then not reliable to estimate the sedimentation

343 accumulation rate. Other explanations for these patterns, such as bioturbation, were considered but  
344 excluded as they differ from the  $^{210}\text{Pb}$  and  $^{226}\text{Ra}$  bioturbation profiles observed in previous studies  
345 (Sakaguchi et al., 2011). For stations 5, 10 and 12, sediment accumulation rates ranged from 47 to 61  
346  $\text{cm kyr}^{-1}$  (Table 1). For station 8, considering only the first two levels of the profile, it was possible to  
347 calculate a sedimentation rate of  $58 \text{ cm kyr}^{-1}$ , close to those obtained at the other stations.

## 348 4 Discussion

349 Sediment traps have been a standard tool for measuring sinking particle fluxes for decades, but  
350 uncertainties remain as to their collection efficiency (e.g., Baker et al., 2020; Buesseler et al., 2007; Butman,  
351 1986; Gardner, 1980; Hargrave and Burns, 1979). In the present study, efforts were made to accurately  
352 collect sinking particles as detailed in *Text S1*.

### 353 4.1 Non-vertical sinking of particles collected in the fixed sediment trap

354 The peaks of the different fractions composing the material were not simultaneously observed in the  
355 traps deployed at 200 and 1000 m at the same site (*Fig. 2*), as usually occurs in similar studies (e.g.,  
356 Guieu et al., 2005; McCave, 1975; Wefer and Fischer, 1993). The temporal shift of these peaks would  
357 indicate that particles would be collected at 1000 m, 30 to 56 days after being collected at 200 m (see  
358 relevant peaks in *Figure S7*). This observation suggests that while sinking toward the seafloor, the  
359 particles were subject to horizontal transport, in view of the westward main current (Tilliette et al.,  
360 2022). Thus, the collected particles sank progressively from the photic layer near the arc (0-150 m)  
361 while being horizontally advected toward the location of the fixed mooring. The time lag between the  
362 collection of particles at 200 and 1000 m is due to depth-dependent physical dynamics (faster current  
363 velocity at surface and influence of mesoscale structures predominant in the sub-region; Rousselet et  
364 al., 2018) as well as the travel time of the water masses, much faster at 200 m than at 1000 m. Indeed,  
365 Lagrangian simulations through Ariane software showed that sinking particles originating from the  
366 Tonga Arc require 61 and 103 days to reach the fixed trap site at 200 and 1000 m, respectively (Grima,

367 pers. comm., 2022). This is consistent with the time lag between the observed peaks at 200 and 1000  
368 m. This reasoning suggests that an important portion of the sinking material collected in the sediment  
369 traps at station 12 would originate from the photic layer near the Tonga Arc, influenced by shallow  
370 hydrothermal fluids, as discussed in Section 4.3. Nevertheless, the finding of a non-vertical sinking of  
371 suspended particles highlights the importance of employing numerous precautions when interpreting  
372 sediment trap data, especially when estimating POC transfer efficiency, which would then be  
373 completely spurious in such a case.

## 374 **4.2 Biogenic components of sinking particles and seafloor sediments during the austral** 375 **summer**

### 376 *4.2.1 Summary of production at studied stations during austral summer conditions*

377 During the TONGA cruise in the austral summer (Bonnet, pers. comm., 2022), high rates of primary  
378 production (PP) were estimated in the Lau Basin (up to  $145 \text{ mmol C m}^{-2} \text{ yr}^{-1}$  at station 10; *Table S3*).  
379 This production was largely supported by cyanobacteria (~70% of total chlorophyll-*a*), primarily  
380 diazotrophs such as *Trichodesmium* that led to high  $\text{N}_2$  fixation rates (up to  $2727 \text{ } \mu\text{mol N m}^{-2} \text{ d}^{-1}$  at  
381 station 5). A significant contribution of coccolithophores was also estimated (~25%) while diatoms  
382 and dinoflagellates represented less than 10% of total chlorophyll-*a* in the Lau Basin. In comparison,  
383 PP and  $\text{N}_2$  fixation were much lower at station 8 ( $< 35 \text{ mmol C m}^{-2} \text{ d}^{-1}$  and  $225 \text{ } \mu\text{mol N m}^{-2} \text{ d}^{-1}$ ,  
384 respectively) and supported predominantly by non-diazotrophic cyanobacteria (Bonnet, Guieu et al.,  
385 2023).

### 386 *4.2.2 Calcium carbonate*

387 The dominant source of  $\text{CaCO}_3$  (mainly calcite) comes from a wide variety of pelagic organisms such  
388 as coccolithophores and foraminifera (Morse et al., 2007). The high  $\text{CaCO}_3$  contents measured at all  
389 stations in sediment traps during the austral summer were consistent with the high productivity of the  
390 Lau Basin estimated at the same period (see section 4.2.1). Interestingly, more  $\text{CaCO}_3$  was collected at  
391 1000 m than at 200 m, certainly due to the fast sinking rates of  $\text{CaCO}_3$  skeletons (Turner, 2002; Zhang

392 et al., 2018; Ziveri et al., 2000). The high levels of CaCO<sub>3</sub> measured in the seafloor sediments at station  
393 12 suggest good preservation of the sinking material on the seafloor in agreement with values reported  
394 in the literature from the region (Table 1; Zhang et al., 2022). The lower CaCO<sub>3</sub> preservation in the  
395 seafloor sediments at station 8 can easily be explained by the seafloor depth (5326 m), far below the  
396 calcite compensation depth (CCD; *Fig. S8*). Conversely, the seafloor at stations 5 and 10 (~2000 m),  
397 located above the lysocline and therefore the CCD, cannot explain the observed patterns. As the Tonga  
398 Arc harbors an intense hydrothermal activity (see section 1), its seafloor may be characterized by strong  
399 physical and chemical gradients (temperature, oxygen levels, multiple forms of chemical energy) and  
400 encompass a diverse range of habitats for microbial life (Karl, 1995). It would thus harbor enormous  
401 biomasses and productivities relative to other regions of the deep ocean (Zierenberg et al., 2000), which  
402 may explain the low CaCO<sub>3</sub> content of the sediments at stations 5 and 10.

#### 403 4.2.3 *Opal*

404 Opal minerals originate from a wide variety of silica-skeleton organisms, primarily diatoms (Tréguer  
405 et al., 1995). As expected from the low proportion of diatoms during the austral summer in the region  
406 (see section 4.2.1), the opal fraction was the least abundant fraction in the sinking material during this  
407 season. As for CaCO<sub>3</sub>, the larger quantity of opal collected at 1000 m than at 200 m can be explained  
408 by the rapid fall rate of the opal skeletons (Bodungen et al., 2013; Turner, 2002). In comparison, the  
409 greater proportion of opal found in the seafloor sediments may be explained by the higher preservation  
410 efficiency of BSi relative to OM and CaCO<sub>3</sub>; degradation of these other fractions may therefore account  
411 for the increasing opal proportion in sediments (Emerson and Hedges, 1988; Gersonde et al., 2005).  
412 Furthermore, opal sinks at rates fast enough to contribute significantly to seafloor sediments, in contrast  
413 to other biogenic fractions (Sarmiento and Gruber, 2006).

#### 414 4.2.4 Organic matter

415 The abundant proportion of OM collected in all traps during the austral summer can easily be linked  
416 to the seasonal productivity of the Lau Basin, which hosts shallow hydrothermal sources driving a  
417 ~360,000 km<sup>2</sup> productivity hotspot, mainly supported by diazotrophs such as *Trichodesmium* (up to  
418 84% of total export; Bonnet, Guieu et al., 2023). This large export matched well with the export of  
419 lithogenic material, except during the austral winter period despite the high supply of lithogenic  
420 material throughout the year. This may be linked to the thermal fitness of *Trichodesmium*, which only  
421 grows at temperatures > 25 °C (Carpenter and Capone, 1992), reached in the Lau Basin between  
422 September and April (Fig. 2f, h). Thus, the high amount of OM exported in the Lau Basin appears to  
423 depend on lithogenic-derived nutrient inputs, suggesting that this material, most likely of hydrothermal  
424 origin (Bonnet, Guieu et al., 2023; Tilliette et al., 2022), would drive the high diazotroph-mediated  
425 production. As expected, only a minor proportion of OM was sequestered in the seafloor sediments,  
426 this material being remineralized during its transport to the deep ocean (Boyd and Trull, 2007 and  
427 reference therein).

428 Taken together, these data illustrate the high biological productivity previously reported in the Lau  
429 Basin during the austral summer season and mainly supported by calcareous (i.e., CaCO<sub>3</sub>) and  
430 diazotrophic (i.e., OM) species (Bonnet, Guieu et al., 2023). These biological particles were intimately  
431 linked to the influx of lithogenic material largely originating from the Tonga Arc, renowned for its  
432 shallow hydrothermal activity (e.g., Massoth et al., 2007; Tilliette et al., 2022). This suggests that  
433 surface production is closely linked to hydrothermal supply in the Lau Basin photic layer. To confirm  
434 the implication of hydrothermalism in triggering the biological response, the origin of lithogenic  
435 particles will be resolved in the subsequent section.

#### 436 4.3 Characteristics of the metallic component in sinking particles and seafloor sediments

437 **4.3.1 Origin of trace metals in sinking particles and link with surface biology**

438 Likely largely originating from the Tonga Arc area (see section 4.1), the lithogenic material collected  
439 in sediment traps was highly enriched in several metals compared to reference pelagic clays. Given the  
440 preponderance of shallow and deep hydrothermal sources in the Lau Basin (e.g., Anderson et al., 2021;  
441 Baker et al., 2019; Beaulieu and Szafranski, 2020; Lupton et al., 2004; Massoth et al., 2007; Tilliette  
442 et al., 2022) and the similar patterns of biological and lithogenic fractions during the austral summer  
443 period, the question of the origin of this metal excess is of utmost interest.

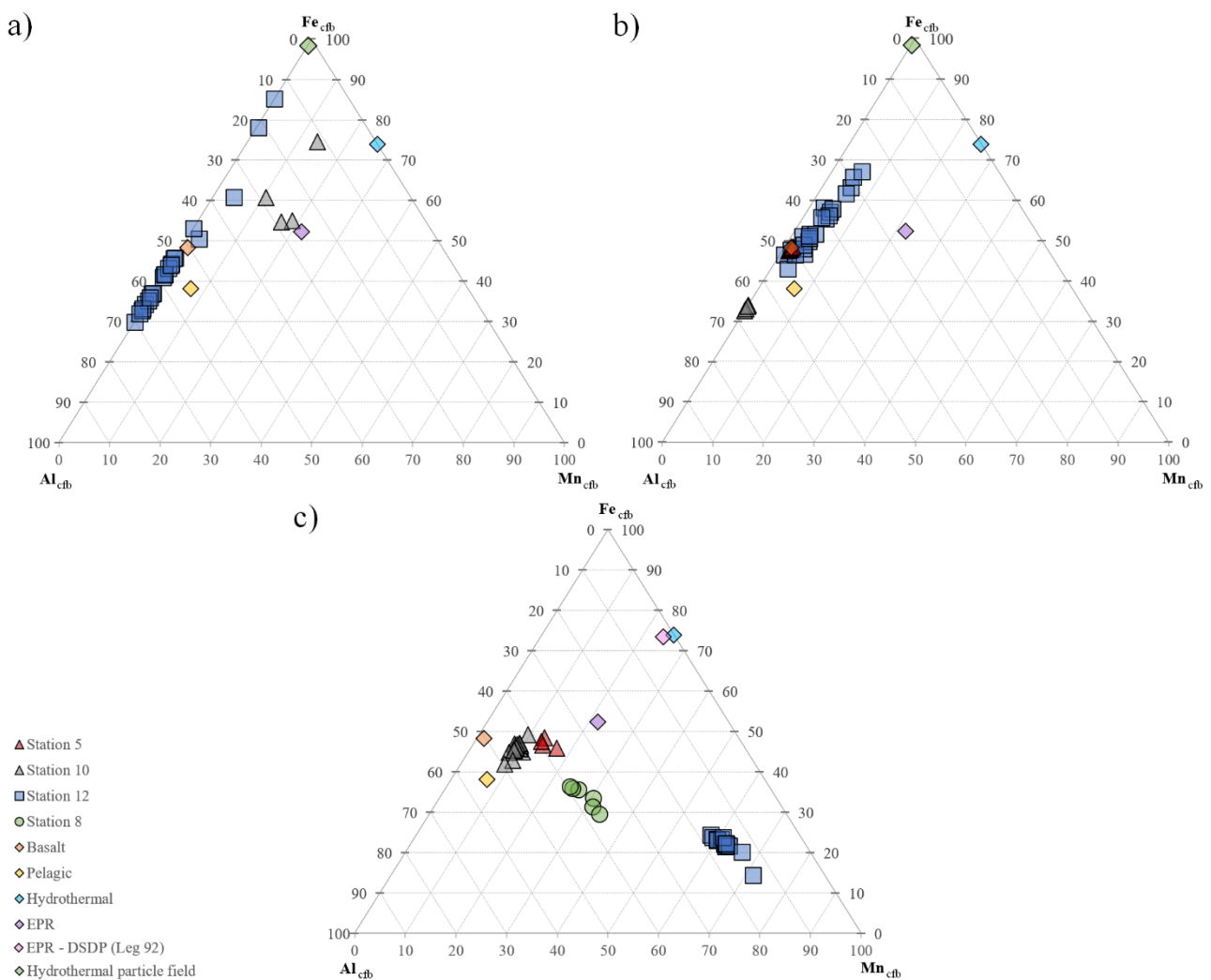
444 **Table 3.** Average Boström indexes measured in sinking particles and seafloor sediments for each station.

Station	Depth (m)	Boström index	
-	-	mean	sd
Station 5	1000	50.6	0.4
	Seafloor	39.7	1.7
	200	23.8	6.1
Station 10	1000	66.6	0.5
	Seafloor	45.2	1.3
	200	55.6	9.7
Station 12	1000	42.7	6.0
	Seafloor	15.9	0.9
Station 8	Seafloor	37.8	1.0

445 *Note.* Indexes were measured as follows:  $100 \times [Al_{cfb} / (Al_{cfb} + Mn_{cfb} + Fe_{cfb})]$  (Boström et al., 1969). The index for detrital  
446 pelagic sediments is 66 (Kyte et al., 1993; Plank et al., 2007). An index below 45 reflects fallout from a dispersed  
447 hydrothermal plume, having a high contribution of Fe-Mn oxides mixed with decreasing proportions of detrital  
448 material as distance from the source decreases (Chavagnac et al., 2008; Dymond, 1981). An index below 15 reflects  
449 near-vent sulfide debris (Mills et al., 1993). The set of index values in each trap cup and sediment slice is available  
450 in the supplementary material (*Table S4*).

451 Hydrothermal material has a particular signature characterized by low Al content but rich in Fe and  
452 Mn, as well as many other metals such as Cu, Zn, Ni and Pb (Boström et al., 1969; Boström and  
453 Peterson, 1969; Cronan, 1972). However, particularities exist for these elements, as some of them, such  
454 as Cu and especially Ni and Zn, decrease dramatically with distance from the source relative to Fe, due  
455 to their rapid removal by sulfide-bearing phases (Trocine and Trefry, 1988). A convenient way to  
456 discriminate material of hydrothermal origin is based on the Boström index using  $Al_{cfb}$ ,  $Fe_{cfb}$  and  $Mn_{cfb}$

457 concentrations (Boström et al., 1969). Its value provides a clear indication of the material provenance:  
 458 a value close to 66 would indicate a clastic detrital sediment (Kyte et al., 1993; Plank et al., 2007) while  
 459 values < 45 would indicate a significant hydrothermal component (Chavagnac et al., 2005; Humphris  
 460 et al., 1995; Mills and Elderfield, 1995). The closer the value is to 0, the more hydrothermal the material  
 461 is and thus the closer the hydrothermal source (Dymond, 1981; Mills et al., 1993). In this study, indexes  
 462 with particular and diverse signatures were determined, suggesting a hydrothermal origin, remote or  
 463 not, of the lithogenic material collected at some of the stations studied (*Table 3*).



464

465 **Figure 5.**  $Fe_{cfb}$ ,  $Mn_{cfb}$  and  $Al_{cfb}$  ternary diagrams for sinking material collected at (a) 200 m and (b) 1000 m and for  
 466 (c) seafloor sediments. Also shown for comparison are some reference materials such as basalt (Japan Basalt, GSJ;  
 467 Imai et al., 1995), reference pelagic clays (see *Table 2*), a hydrothermal vent solution (Li and Schoonmaker, 2003), a

468 reference sedimentary material from the East Pacific Rise (EPR; Barrett et al., 2021; Nohara and Yokoto, 1978) and  
469 a hydrothermal particle field (Edmonds and German, 2004).

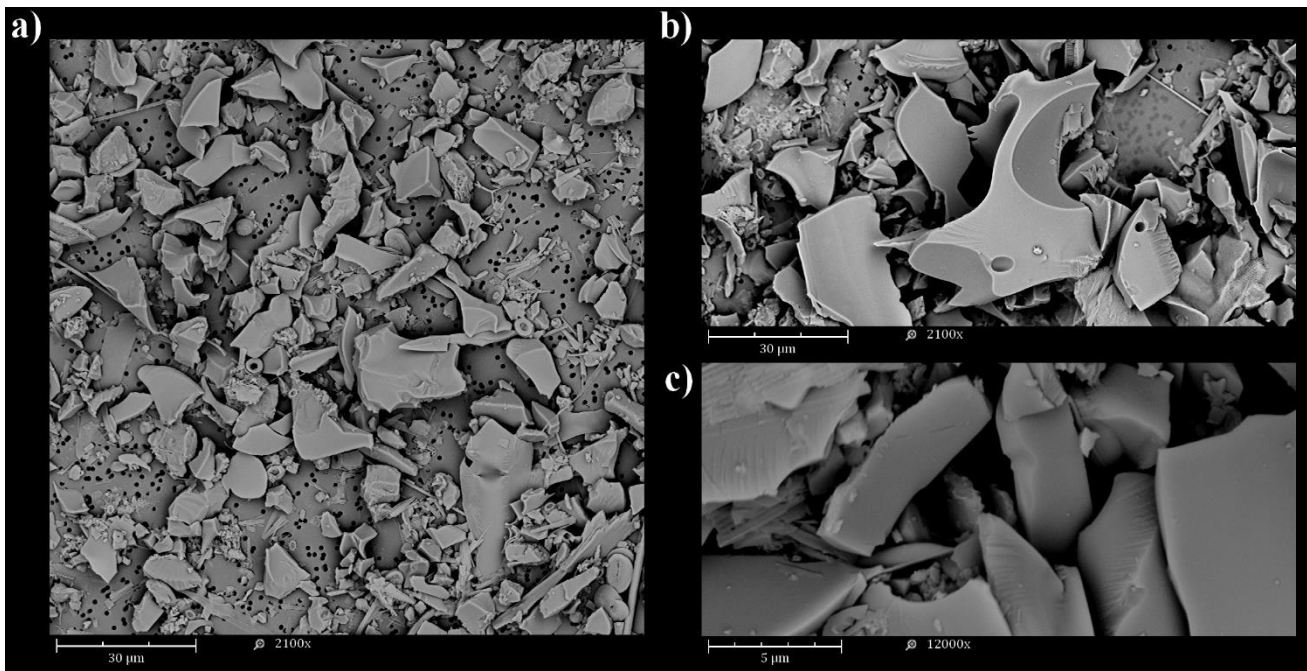
#### 470 *4.3.1.1 Along the Tonga Arc (small scale)*

471 Stations 5 and 10 are located along the Tonga Arc, which hosts a multitude of active hydrothermal  
472 vents (e.g., Beaulieu and Szafranski, 2020; Lupton et al., 2004; Massoth et al., 2007). About 15 km  
473 from the location of each of the drifting mooring lines, a shallow hydrothermal source was identified  
474 during the TONGA cruise at ~300 m at station 10 and at ~200 m at station 5 (Tilliette et al., 2022).

475 *Station 10.* Station 10 revealed materials with distinctive signatures depending on sampling depth. At  
476 200 m, the Boström index revealed a clear signature of a fairly close hydrothermal source with Fe-Mn-  
477 rich lithogenic particles (*Table 3, Fig. 5a*), similar to metalliferous sediments sampled downstream of  
478 the Rain hydrothermal vent on the Mid-Atlantic ridge (Cave et al., 2002). Such index is in agreement  
479 with the identification, ~15 km away from the drifting mooring initial position, of a shallow source  
480 exhibiting multiple acoustic anomalies and high DFe concentrations (Tilliette et al., 2022).  
481 Consistently, Cu<sub>EF</sub>, Zn<sub>EF</sub> and Ni<sub>EF</sub> were detected in the trap (*Table 2*). However, biological  
482 (intracellular) inputs through OM must partly contribute to these high enrichments, since some metals,  
483 notably Zn, are highly abundant in phytoplankton ( $[C_{106}N_{16}P_1]_{1000}Fe_{11.9}Zn_{1.27}Cu_{0.15}$ ; Ho et al., 2003;  
484 Redfield et al., 1963; Zhang et al., 2018). Based on these elemental ratios, the contribution of the  
485 biological fraction to Zn<sub>EF</sub> can be considered negligible (~3%). Nevertheless, all these arguments point  
486 out to a hydrothermal origin of a large part of the lithogenic material collected at 200 m, which likely  
487 triggered surface biological production at this station during the austral summer.

488 At 1000 m, a Boström index typical of conventional detrital material was measured (*Table 3*), although  
489 the Al-Fe-Mn signature of the collected material seems to differ from that of the reference pelagic clays  
490 (*Fig. 5b*). Yet, station 10 is located close to the Late'iki submarine volcano, which erupted a month  
491 prior to the cruise. This surtseyan eruption created a new island, baptized New Late'iki, which eroded

492 in just two months. This erosion released a large amount of volcanic material into the water column,  
493 which was detectable until December 2020 (Plank et al., 2020). Accordingly, a large abundance of  
494 basaltic glass, likely from this eruption, was collected in the 1000 m-trap deployed at this station (*Fig.*  
495 *6*). Indeed, the angular shape of this volcanic material indicates its recent origin and freshness, since  
496 remobilized volcanic particles would display more rounded angles. The detrital-like Boström index  
497 can therefore be attributed to the predominance of volcanic-derived particles, a material reported as  
498 Mn-poor but Fe and Al-rich (*Fig. 5b*; e.g., Almirón et al., 2021; Fiantis et al., 2010; Leonelli et al.,  
499 2007; Naji and Asi, 2008; Oskarasson, 2010; Razzhigaeva et al., 2009; Tchakoute Kouamo et al.,  
500 2012).  $LSi_{EF}$  at 1000 m provides further evidence, as this element has been reported to be enriched in  
501 volcanic material relative to pelagic ones (Li and Schoonmaker, 2003; Sayles and Bischoff, 1973;  
502 Bailey, 1993; Fiantis et al., 2010). Thus, a mixture of volcanic, hydrothermal and detrital material  
503 probably prevailed at 1000 m. Given the large amount of material ejected following the Late'iki  
504 eruption and the biological response to lithogenic inputs in the austral summer, it is interesting to  
505 consider a possible co-fertilization of biology by both hydrothermal and volcanic processes. However,  
506 such volcanic fertilization is unlikely as no volcanic signature was detected in the 200 m-trap (i.e., no  
507  $LSi_{EF}$ ) and recent studies in the region have demonstrated that volcanic material, particularly basaltic  
508 glass, is poorly bioavailable and does not generate a significant biological response (Whiteside et al.,  
509 2023, 2021).



510

511 **Figure 6.** Scanning electron microscopy views of dry material from samples collected in the 1000 m-trap at station  
 512 10 where basaltic glass was recovered (magnification **(a, b)**: x2,100 and **(c)**: x12,000).

513 *Station 5.* The shallow hydrothermal source identified at ~200 m at station 5 during the TONGA cruise  
 514 was a very active site showing typical acoustic and chemical anomalies such as low pH, low O<sub>2</sub>  
 515 concentrations and high levels of DFe, DMn, CH<sub>4</sub>, CO<sub>2</sub> and H<sub>2</sub>S (Tilliette et al., 2022). At 1000 m, the  
 516 moderate Boström index of the collected lithogenic particles likely reflected a mixture of **(1)**  
 517 hydrothermal material from shallow hydrothermal plumes (Tilliette et al., 2022), notably supported by  
 518 strong Fe<sub>EF</sub> and Zn<sub>EF</sub> (*Table 2, Fig. 5b*), **(2)** volcanic material from New Late'iki erosion, according to  
 519 the westward main current, supported by LSi and Al enrichments as well as Mn depletion (*Fig. 5b,*  
 520 *Table 2*) and **(3)** detrital material. Thus, the lithogenic material collected at 1000 m appears to have  
 521 both volcanic and hydrothermal origins. As volcanic material is poorly bioavailable (Whiteside et al.,  
 522 2023, 2021), it can be concluded that the large quantities of biological material collected during the  
 523 austral summer, in particular OM and CaCO<sub>3</sub>, result from the presence of a shallow hydrothermal  
 524 source along the Tonga Arc (Tilliette et al., 2022). This source released high amounts of lithogenic  
 525 material rich in numerous metals essential for phytoplankton growth, such as Fe, thereby sustaining

526 significant biological productivity. However, as the 200 m-trap did not work (see section 2.1), its  
527 deployment needs to be renewed to confirm that the hydrothermal material identified at 1000 m  
528 originates exclusively from the near-surface source identified, or whether additional deeper sources  
529 exist.

#### 530 *4.3.1.2 Along the Lau ridge (large scale)*

531 Station 12 was positioned sufficiently far from the identified shallow hydrothermal sources on the  
532 Tonga Arc to incorporate their effect on a regional scale. At 200 m, the lithogenic material collected  
533 exhibited a rather high Boström index, but still lower than detrital material, reflecting the likely remote  
534 impact of the shallow sources identified along the Tonga Arc (~200 km from station 12). These sources  
535 supply low but still significant concentrations of metals up to the photic layer of the Lau Ridge,  
536 particularly Fe (*Fig. 5a*), in line with the main westward current reflecting their impact on a regional  
537 scale. The Boström index variability over the year suggests an important role of subsurface dynamics  
538 in delivering lithogenic material up to station 12 (Table S4). Consistent with this distal hydrothermal  
539 contribution, no  $\text{Cu}_{\text{EF}}$  and  $\text{Ni}_{\text{EF}}$  were detected in this trap. Similar to station 10, a small proportion of  
540 the  $\text{Zn}_{\text{EF}}$  estimated at station 12 can be partially attributed to OM supplies (up to 2% biologically-  
541 derived Zn, depending on the collection period). Thus, the lithogenic material collected at 200 m at  
542 station 12 appears to have a hydrothermal origin, similarly to the stations along the Tonga Arc. This  
543 observation suggests that hydrothermal inputs from the Tonga Arc into the photic layer can fertilize  
544 surface biology on the scale of an entire ocean basin (i.e., from the Tonga Arc to the Lau Ridge – 200  
545 km), as long as the optimal conditions for diazotroph growth (i.e., temperature), reached during the  
546 austral summer period in the region, are satisfied.

547 The lower Boström index measured at 1000 m than at 200 m at station 12 reflects a greater influx of  
548 hydrothermal material, especially Fe, from distal shallow and/or deep source(s) likely located along  
549 the Tonga Arc (*Fig. 5b, Table 3*). A part of the lithogenic particles collected were also of volcanic

550 origin, in view of the Mn depletions as well as Al, Fe and LSi enrichments, thus impacting the measured  
551 index (i.e., increasing it). These LSi<sub>EF</sub> likely originated from the Late'iki eruption (mid-October 2019;  
552 Plank et al., 2020) and the subsequent fast erosion of the newly created island (within two months post-  
553 eruption), consistent with the main western current potentially carrying basaltic glass to station 12  
554 (Tilliette et al., 2022). This hypothesis is supported by the travel time of particles from station 10 (about  
555 15 km away from New Late'iki) to the fixed trap site at station 12 estimated to be about a hundred days  
556 at 1000 m by the Ariane Lagrangian dispersion tool (Grima, pers. comm., 2022; see Section 4.1).  
557 Indeed, no LSi<sub>EF</sub> was detected at 1000 m at station 12 about 150 days after the submarine volcano  
558 eruption ( $x0.4 \pm 0.3$  between March and October 2020), and about 70 days after the island  
559 disappearance due to erosion, in agreement with the estimated dispersal times at 1000 m from the  
560 Tonga Arc to the fixed mooring site. Thus, as for station 5, the lithogenic material collected at 1000 m  
561 is derived from volcanism as well as from shallow and/or deep hydrothermalism. However, only  
562 material of hydrothermal origin may explain the substantial biological production measured remotely  
563 of the Tonga Arc during the austral summer period.

#### 564 **4.3.2 Origin of trace metals in sediments**

565 Mirroring the material collected in sediment traps, the lithogenic material collected in the sediments  
566 was highly enriched in metals. Given the intense hydrothermal and volcanic activity prevalent in the  
567 region (see section 4.3.1 and references therein), it is important to question the potential origins of  
568 these metal excesses, in particular to determine whether or not the sources feeding the sediments differ  
569 from those feeding the water column.

##### 570 *4.3.2.1 In the Lau Basin*

571 *Station 10.* In the sediments at station 10, a lower Boström index than that of material collected at 1000  
572 m indicated the presence of a deep (> 1000 m), rather distal, hydrothermal source feeding the sediments  
573 with high Fe, Cu and, to a lesser extent, Mn contents (*Table 3, Figs. 3, 5c*). Indeed, although volcanic

574 material (i.e., increasing the index) was also present within the sediments according to  $LSi_{XS}$  estimates,  
575 the decrease of the index value seems to indicate additional hydrothermal input at depths > 1000 m.  
576 The source(s) of these inputs appear(s) to be at a reasonable distance from the station, given the particle  
577 size typical of distal transport (1-100  $\mu\text{m}$ ; Feely et al., 1990, 1987; Lou et al., 2020). Consistently,  
578 estimated sedimentation rates were 94-470 times higher than those of pelagic sediments (average 0.1-  
579 0.5  $\text{mm kyr}^{-1}$ ; Li and Schoonmaker, 2003; Piper, 2005) and in the range of those measured in  
580 hydrothermally-influenced areas accumulating to several  $\text{cm kyr}^{-1}$  (Cave, 2002; Cave et al., 2002;  
581 Dutkiewicz et al., 2016; Mahiques et al., 2011). Such rates indicate a significant material flux, likely  
582 from hydrothermal and volcanic origin. It is important to note that the recovery within the sediments  
583 of the volcanic signature identified at 1000 m is not surprising, as this volcano is known for its recurrent  
584 eruptions since the 18<sup>th</sup> century (Ewart et al., 1977), in line with  $LSi_{XS}$  estimates at depths > 3 cm below  
585 the seafloor (corresponding to the 18th century; see *Table 1*).

586 *Station 5.* The sediments at station 5 showed a medium Boström index, but lower than that estimated  
587 in the material collected at 1000 m, possibly due to the additional distal impact of deeper sources (>  
588 1500 m; Tilliette et al., 2022), feeding the sediments with high  $Fe_{XS}$ ,  $Mn_{XS}$  and  $Cu_{XS}$  (*Figs. 3, 5c, Table*  
589 *3*). This distal hydrothermal origin was also supported by **(1)** the heterogeneous and large size of  
590 particles, much larger than clays (< 3  $\mu\text{m}$ ; Horn et al., 1970; Leinen, 1989) and typical of distal transport  
591 (Feely et al., 1990, 1987; Lou et al., 2020; Ng et al., 2019), **(2)** the accumulation rates much higher  
592 than those of pelagic clays (x116-580; Li and Schoonmaker, 2003; Piper, 2005) and finally **(3)** the  
593 absence of  $Ni_{XS}$  and  $Zn_{XS}$  throughout the core (*Fig. 3*), these elements being lost near sources. The  
594 presence of volcanic material (i.e., increasing the index value) is also strongly suspected in the  
595 sediments of this station, in view of the estimated continuous  $LSi_{XS}$  (sampled core dating from the 19th  
596 century to the present day according to accumulation rates, see *Table 1*) and the frequent eruptions of  
597 the Late'iki volcano since the 18th century (Ewart et al., 1977).

598 The very low Boström index of the sediments at Station 12 reflects a strong hydrothermal signature of  
599 a likely near-vent field with material exhibiting high  $\text{Fe}_{\text{XS}}$  and  $\text{Mn}_{\text{XS}}$  (Table 3, Figs. 3, 5c). Although  
600 this result was unexpected, the presence of a nearby source at the seafloor of station 12 is supported by  
601 the high accumulation rates ( $\times 122\text{-}610$  relative to pelagic clays; Li and Schoonmaker, 2003), the  
602 particle size distribution, with grain up to  $976\ \mu\text{m}$ , typical of near-vent debris (Feely et al., 1990, 1987;  
603 Lou et al., 2020; Ng et al., 2019) as well as the high  $\text{Zn}_{\text{XS}}$ ,  $\text{Ni}_{\text{XS}}$  and  $\text{Cu}_{\text{XS}}$ . Additional arguments in  
604 favor of the presence of strong hydrothermal activity in the vicinity of this station would be (1) the  
605 numerous reports of discolored waters and volcanic activity according to nautical charts of this area  
606 (SHOM C, 6817, INT605), (2) many potential active volcanic structures ( $> 1000\ \text{m}$ ; GEBCO  
607 Bathymetric Compilation Group, 2022), and (3) a mega-plume hypothesized within few kilometers of  
608 the station ( $20^{\circ}28'\ \text{S}$ ,  $178^{\circ}31'\ \text{W}$ ), near the Lau Ridge (Guieu et al., 2018). It should be noted that no  
609  $\text{LSi}_{\text{EF}}$  was estimated in these sediments, revealing that the large particle sizes estimated in this study  
610 originate solely from hydrothermal processes, consistent with the high Mn and low Al content.

#### 611 4.3.2.2 *In the South Pacific gyre*

612 Station 8 is located east of the Tonga Arc and was initially cored as a deep-sea detrital reference.  
613 However, the sediment index reveals a distal hydrothermal signature, as evidenced by high  $\text{Fe}_{\text{XS}}$ ,  $\text{Mn}_{\text{XS}}$ ,  
614  $\text{Cu}_{\text{XS}}$  and, to a lesser extent,  $\text{Pb}_{\text{XS}}$  (Figs 3, 5), although the estimated elemental excess were lower than  
615 in the Lau Basin. Consistent with these observations, the estimated sedimentation rates were  $116\text{-}580$   
616 times higher than those of pelagic sediments (Li and Schoonmaker, 2003; Piper, 2005), indicating a  
617 great material flux. It is possible that this material originated from the east, for example from the East  
618 Pacific Rise and/or other nearby deep hydrothermal source(s) (Kipp et al., 2018; Resing et al., 2015),  
619 although no DFe anomalies were detected in the deep waters at this station relative to DFe  
620 concentrations in water masses feeding the gyre region, albeit possibly due to the high threshold  
621 defined in that study ( $= 0.2\ \text{nmol L}^{-1}$ ; Tilliette et al., 2022). This hypothesis is supported by the particle

622 size falling within the range of hydrothermal particles involved in long-distance transport (1-50  $\mu\text{m}$ ;  
623 Feely et al., 1990, 1987; Lou et al., 2020). In addition, hydrothermal plumes have been reported to be  
624 transported thousands of kilometers away from their source at the ridge axis (Resing et al., 2015) and  
625 result in continuous fallout of metals over large distances (Lilley et al., 2013), possibly up to station 8.  
626 Furthermore, Boström et al. (1969) also demonstrated the presence of sediments influenced by distal  
627 hydrothermalism near this site.

#### 628 4.3.2.3 Detrital component

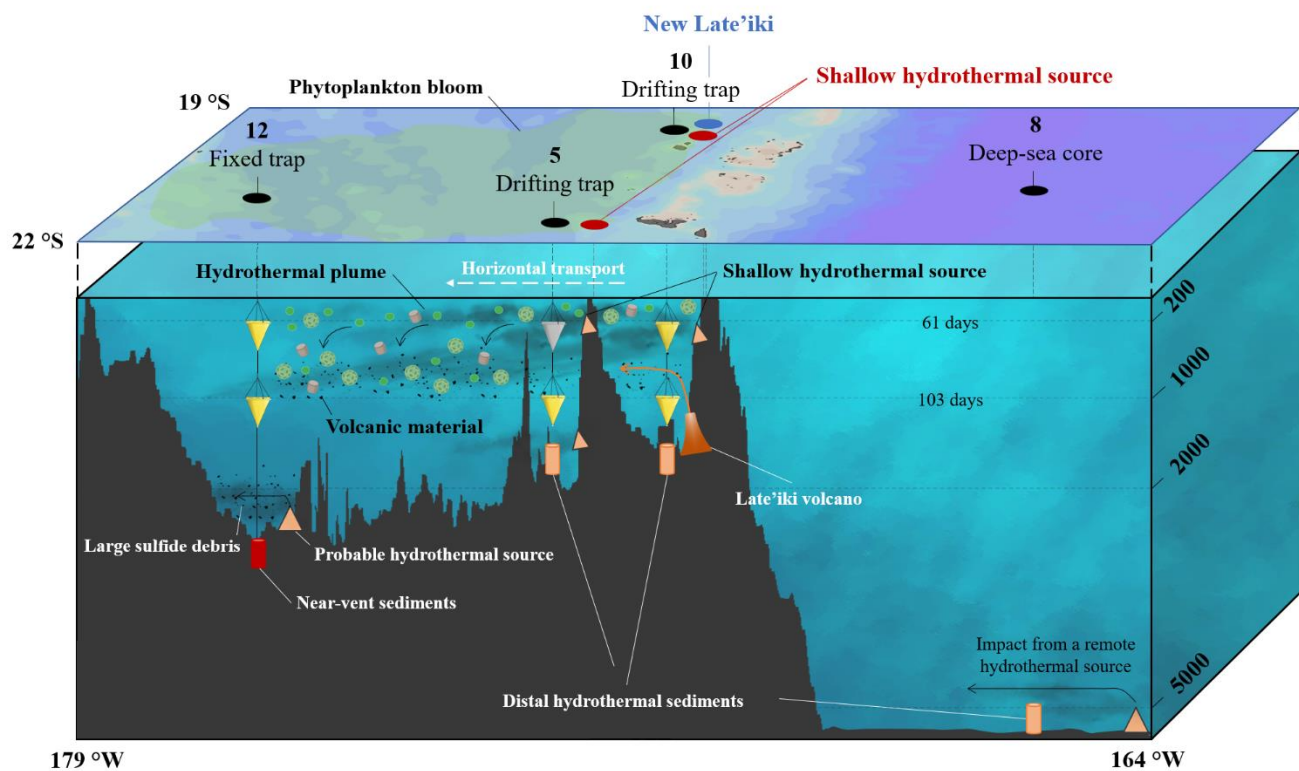
629 As described in section 4.3.1, microscopic inspection of particles collected in sediment traps at 1000  
630 m reveals the occurrence of a large abundance of basaltic glass, as evidenced by the sharp angle of  
631 large-sized particles. Escrig et al. (2012) collected fresh volcanic glass along the latitudinal location of  
632 the Fonualei Spreading Center (between  $-18^\circ$  and  $-16^\circ\text{S}$ ) corresponding to an end-member of global  
633 back-arc lavas in the Lau Basin. These volcanic glasses exhibit average (Fe/Mn) ratio and Si content  
634 of  $54 \pm 5$  and  $25 \pm 1$  wt.%, respectively. Here, we were able to determine the geochemical composition  
635 of the detrital material based on geochemical features measured in the seafloor sediments. Following  
636 the calculations presented in section 2.4.2, the average detrital fraction is characterized by  $(\text{Fe/Mn})_{\text{det}}$   
637 and  $\text{Si}_{\text{det}}$  at  $54 \pm 3$  and  $22 \pm 5$  wt.%, respectively. These chemical signatures are extremely similar to  
638 those of the volcanic glasses analyzed by Escrig et al. (2012) as well as for trace metal such as Ni.  
639 Nevertheless, the detrital fraction is 10 and 2 times more enriched in Pb and Zn, respectively. This  
640 suggests that the hydrothermal contribution has been underestimated, as mentioned in section 2.4.2,  
641 since hydrothermalism is the only explanation for such strong enrichments (Adams et al., 2006; Canion  
642 and Landsberger, 2013; Taylor, 1964). Overall, the detrital fraction identified, observed and analyzed  
643 here exhibits morphology and geochemical features that are consistent with a nearby volcanic origin  
644 solely.

## 645 5 Conclusion

646 In this study, deployment of sediment traps and coring of seafloor sediments allowed the identification  
647 and characterization of biogenic and hydrothermally-derived particles along the Tonga Arc over large  
648 spatio-temporal scales, from the Lau Ridge to the western border of the South Pacific gyre (along ~20  
649 °S; *Fig. 7*). Consistent with the high biological productivity previously reported in the Lau Basin, large  
650 quantities of biogenic material (organic matter, opal and calcium carbonate) were collected at 200 and  
651 1000 m during the austral summer period. These particles were intimately related to the influx of  
652 lithogenic material from the Tonga Arc, whose hydrothermal origin could be resolved through  
653 numerous geochemical tracers (Al, Ca, Cu, Fe, Mn, Ni, Pb, Si, Zn). Such a result suggests that surface  
654 production is tightly linked to hydrothermal supply within the Lau Basin photic layer. Seafloor  
655 sediments from all stations also exhibited a metal-rich hydrothermal signature (Fe, Mn-rich, Al-  
656 depleted), supported by their high accumulation rates as well as the coarse and heterogeneous size of  
657 the sedimented particles, typical of hydrothermal oxide and/or sulfide debris. Thus, the sinking and  
658 sedimented particles were primarily from shallow to deep hydrothermal sources identified along the  
659 Tonga Arc. This set of evidence supports a major influence of hydrothermal sources and refutes the  
660 island effect often considered in this region.

661 Shallow and/or deep hydrothermal sources impacted the composition of sinking and sedimented  
662 particles at all stations sampled in the Lau Basin. The effect of the sources on the particle signature  
663 depended on their distance from the sampled site. The signature of hydrothermal material was  
664 pronounced in the sediment traps deployed at stations 5 and 10 (~15 km from the arc and identified  
665 shallow sources). It was also revealed but to a lesser extent at station 12, located near the Lau Ridge  
666 (~200 km from the arc), and was primarily reflected through Fe enrichments in the water column both  
667 at the surface (200 m) and at depth (1000 m). At all stations, besides the impact of hydrothermalism, a  
668 volcanic signature (Fe, LSi, Al-rich, Mn-depleted) was identified in the particles collected in the  
669 deepest sediment trap. This abundant volcanic material probably originated from the recent eruption

670 of the Late'iki submarine volcano and the subsequent fast erosion of the newly created island, as  
 671 confirmed through the observation of basaltic glass in the 1000 m-trap at station 10. Surprisingly, the  
 672 seafloor at station 12 reflects a deep hydrothermal activity, as evidenced by the typical signature of  
 673 sulfide debris found near hydrothermal vents and the large and heterogeneous particle size. At the  
 674 South Pacific gyre deep-sea reference site, the Al-Fe-Mn tracing in the seafloor sediments detected the  
 675 distal impact of a deep hydrothermal source, likely present along the East Pacific Rise.



676 179 °W 164 °W

677 **Figure 7.** Summary diagram of the main results of the present study. These include (1) the non-vertical sinking of  
 678 particles; (2) the impact of shallow hydrothermal plumes on all sediment traps in the Lau Basin; (3) the impact of  
 679 volcanic material from the Late'iki volcano eruption on the deep traps deployed at stations 5, 10 and 12; (4) the impact  
 680 of shallow and deep hydrothermalism, along with submarine volcanism, on seafloor sediments; (5) the impact of a  
 681 distal hydrothermal source on the sediments at the deep-sea reference site; and (6) the impact of the potential deep  
 682 hydrothermal source deduced near station 12. Note that no sample could be collected from the 200 m-trap deployed  
 683 at station 5 (shaded) due to a PPS-5 malfunction. The days shown on the 200 and 1000 m lines indicate the travel  
 684 time of particles from the Tonga Arc to the fixed trap site at these depths.

685 All these data lead to the conclusion that a myriad of shallow and deep hydrothermal sources, located  
686 along the Tonga Arc, fertilize the entire Lau Basin with numerous elements, including Fe, triggering  
687 significant POC production during the austral summer period, when the temperature conditions  
688 required for the diazotroph development are fulfilled. These hydrothermal sources, along with  
689 submarine volcanism, have a significant impact on the biogeochemistry of the Lau Basin, at very large  
690 spatial (from the Tonga Arc to the Lau Ridge) and temporal (from seasonal to centennial time scales  
691 in seafloor sediments) scales. This study also illustrates the importance of employing considerable care  
692 in interpreting sediment trap data, as these are certainly influenced by physical dynamics, thus greatly  
693 affecting the vertical sinking of collected particles.

694 Future research is needed to probe the seafloor near station 12 for acoustic and chemical anomalies to  
695 identify the hydrothermal source(s) responsible for the presence of large, metal-rich sedimented  
696 particles. Finally, molecular analyses could be interesting to characterize the different bacteria and/or  
697 archaea present in the water-sediment interface and to draw conclusions on the low CaCO<sub>3</sub> preservation  
698 observed in the seafloor sediments along the Tonga Arc.

## 699 **6 Declaration of Competing Interest**

700 The authors declare that they have no known competing financial interests or personal relationships  
701 that could have appeared to influence the work reported in this paper.

## 702 **7 Acknowledgments**

703 This work was carried out in the framework of the TONGA project (TONGA cruise GEOTRACES  
704 GPpr14, November 2019, <https://doi.org/10.17600/18000884>) managed by the LOV (CG) and the  
705 MIO. The project was funded by the TGIR Flotte Océanographique Française, the A-MIDeX of Aix-  
706 Marseille University, the LEFE-CYBER and GMMC program and the Agence Nationale de Recherche  
707 (ANR-18-CE01-0016). We warmly thank all the scientists, the captain and the crew of the R/V

708 L'Atalante for their cooperative work at sea. We thank the crew of the R/V Alis (TGIR Flotte, operated  
709 by IFREMER) for the safe recovery of the fixed mooring in particularly difficult weather conditions.  
710 We thank Faustine Fauche for her help in the analysis of trap and core samples. We thank the SNAPO-  
711 CO<sub>2</sub> platform for carbonate chemistry analyzes. We thank Christophe Maes and Nicolas Grima for  
712 their help in positioning the fixed mooring line and for the Lagrangian analyses.

## 713 **8 Supplementary Material**

714 Supplementary material to this article is the following: Supplementary information 1 (PDF file)

## 715 **9 Open Research**

716 The data used in this study are publicly available on the SEANOE database (Guieu et al., 2022)  
717 (<http://doi.org/10.17882/88169>).

## 718 **10 References**

- 719 Adams, A., Christiansen, E., Kowallis, B., Carranza-Castañeda, O., Miller, W., 2006. Contrasting  
720 Silicic Magma Series in Miocene-Pliocene Ash Deposits in the San Miguel de Allende  
721 Graben, Guanajuato, Mexico. *The Journal of Geology* 114, 247–266.  
722 <https://doi.org/10.1086/499633>
- 723 Almirón, J., Vargas, M., Tupayachy-Quispe, D., Duquesne, S., Roudet, F., Silva-Vela, A., 2021.  
724 Influence of the Process of Synthesis of Zeolites from Volcanic Ash in Its Synergistic Action  
725 as a Flame-Retardant for Polypropylene Composites. *Buildings* 12, 24.  
726 <https://doi.org/10.3390/buildings12010024>
- 727 Anderson, M.O., Norris-Julseth, C., Rubin, K.H., Haase, K., Hannington, M.D., Baxter, A.T.,  
728 Stewart, M.S., 2021. Geologic and Structural Evolution of the NE Lau Basin, Tonga:  
729 Morphotectonic Analysis and Classification of Structures Using Shallow Seismicity. *Front.*  
730 *Earth Sci.* 9, 665185. <https://doi.org/10.3389/feart.2021.665185>
- 731 Bailey, D.K., 1993. Carbonate magmas. *JGS* 150, 637–651. <https://doi.org/10.1144/gsjgs.150.4.0637>
- 732 Baker, C.A., Estapa, M.L., Iversen, M., Lampitt, R., Buesseler, K., 2020. Are all sediment traps  
733 created equal? An intercomparison study of carbon export methodologies at the PAP-SO site.  
734 *Progress in Oceanography* 184, 102317. <https://doi.org/10.1016/j.pocean.2020.102317>
- 735 Baker, E.T., Walker, S.L., Massoth, G.J., Resing, J.A., 2019. The NE Lau Basin: Widespread and  
736 Abundant Hydrothermal Venting in the Back-Arc Region Behind a Superfast Subduction  
737 Zone. *Front. Mar. Sci.* 6, 382. <https://doi.org/10.3389/fmars.2019.00382>
- 738 Barrett, T.J., Jarvis, I., Hannington, M.D., Thirlwall, M.F., 2021. Chemical characteristics of modern  
739 deep-sea metalliferous sediments in closed versus open basins, with emphasis on rare-earth

- 740 elements and Nd isotopes. *Earth-Science Reviews* 222, 103801.  
741 <https://doi.org/10.1016/j.earscirev.2021.103801>
- 742 Beaulieu, S.E., Szafranski, K.M., 2020. InterRidge Global Database of Active Submarine  
743 Hydrothermal Vent Fields Version 3.4. <https://doi.org/10.1594/PANGAEA.917894>
- 744 Berger, W.H., Smetacek, V., Wefer, G., 1989. Ocean productivity and paleoproductivity - an  
745 overview, in: *Productivity of the Oceans Present and Past*. Wiley, Berlin, pp. 1–34.
- 746 Bodungen, B.V., Wunsch, M., Fürderer, H., 2013. Sampling and Analysis of Suspended and Sinking  
747 Particles in the Northern North Atlantic, in: Hurd, D.C., Spencer, D.W. (Eds.), *Geophysical  
748 Monograph Series*. American Geophysical Union, Washington, D. C., pp. 47–56.  
749 <https://doi.org/10.1029/GM063p0047>
- 750 Bonnet, S., Caffin, M., Berthelot, H., Moutin, T., 2017. Hot spot of N<sub>2</sub> fixation in the western  
751 tropical South Pacific pleads for a spatial decoupling between N<sub>2</sub> fixation and denitrification.  
752 *Proc Natl Acad Sci USA* 114, E2800–E2801. <https://doi.org/10.1073/pnas.1619514114>
- 753 Bonnet, S., Guieu, C., Taillandier, V., Boulart, C., Bouruet-Aubertot, P., Gazeau, F., Scalabrin, C.,  
754 Bressac, M., Knapp, A.N., Cuypers, Y., González-Santana, D., Forrer, H.J., Grisoni, J.-M.,  
755 Grosso, O., Habasque, J., Jardin-Camps, M., Leblond, N., Le Moigne, F.A.C., Lebourges-  
756 Dhaussy, A., Lory, C., Nunige, S., Pulido-Villena, E., Rizzo, A.L., Sarthou, G., Tilliette, C.,  
757 2023. Natural iron fertilization by shallow hydrothermal sources fuels diazotroph blooms in  
758 the ocean. *Science* 380, 812–817. <https://doi.org/10.1126/science.abq4654>
- 759 Boström, K., Peterson, M.N.A., 1969. The origin of aluminum-poor ferromanganoan sediments in  
760 areas of high heat flow on the East Pacific Rise. *Marine Geology* 7, 427–447.  
761 [https://doi.org/10.1016/0025-3227\(69\)90016-4](https://doi.org/10.1016/0025-3227(69)90016-4)
- 762 Boström, K., Peterson, M.N.A., Joensuu, O., Fisher, D.E., 1969. Aluminum-poor ferromanganoan  
763 sediments on active oceanic ridges. *J. Geophys. Res.* 74, 3261–3270.  
764 <https://doi.org/10.1029/JB074i012p03261>
- 765 Boyd, P.W., Trull, T.W., 2007. Understanding the export of biogenic particles in oceanic waters: Is  
766 there consensus? *Progress in Oceanography* 72, 276–312.  
767 <https://doi.org/10.1016/j.pocean.2006.10.007>
- 768 Brzezinski, M.A., Nelson, D.M., 1995. The annual silica cycle in the Sargasso Sea near Bermuda.  
769 *Deep Sea Research Part I: Oceanographic Research Papers* 42, 1215–1237.  
770 [https://doi.org/10.1016/0967-0637\(95\)93592-3](https://doi.org/10.1016/0967-0637(95)93592-3)
- 771 Buesseler, K.O., Antia, A.N., Chen, M., Fowler, S.W., Gardner, W.D., Gustafsson, O., Harada, K.,  
772 Michaels, A.F., Rutgers van der Loeff, M., Sarin, M., Steinberg, D.K., Trull, T., 2007. An  
773 assessment of the use of sediment traps for estimating upper ocean particle fluxes. *J. Mar. Res.*  
774 65, 345–416. <https://doi.org/10.1357/002224007781567621>
- 775 Butman, C.A., 1986. Sediment trap biases in turbulent flows: Results from a laboratory flume study.  
776 *Journal of Marine Research* 44, 645–693. <https://doi.org/10.1357/002224086788403051>
- 777 Canion, B., Landsberger, S., 2013. Trace analysis and leaching dynamics of volcanic ash using NAA  
778 and ICP-MS. *J. Radioanal. Nucl. Chem.* 296, 375–378. [https://doi.org/10.1007/s10967-012-  
779 2069-3](https://doi.org/10.1007/s10967-012-2069-3)
- 780 Carpenter, E.J., Capone, D.G., 1992. Nitrogen Fixation in *Trichodesmium* Blooms, in: Carpenter, E.  
781 J., Capone, D. G., Rueter, J.G. (Eds.), *Marine Pelagic Cyanobacteria: Trichodesmium and*

- 782 Other Diazotrophs, NATO ASI Series. Springer Netherlands, Dordrecht, pp. 211–217.  
783 [https://doi.org/10.1007/978-94-015-7977-3\\_13](https://doi.org/10.1007/978-94-015-7977-3_13)
- 784 Cave, R., 2002. A Geochemical Study of Hydrothermal Signals in Marine Sediments: The Rainbow  
785 Hydro thermal Area, 36 degrees on the Mid-Atlantic Ridge (PhD Thesis). University of  
786 Southampton.
- 787 Cave, R.R., German, C.R., Thomson, J., Nesbitt, R.W., 2002. Fluxes to sediments underlying the  
788 Rainbow hydrothermal plume at 36°14'N on the Mid-Atlantic Ridge. *Geochimica et*  
789 *Cosmochimica Acta* 66, 1905–1923. [https://doi.org/10.1016/S0016-7037\(02\)00823-2](https://doi.org/10.1016/S0016-7037(02)00823-2)
- 790 Chavagnac, V., German, C.R., Milton, J.A., Palmer, M.R., 2005. Sources of REE in sediment cores  
791 from the Rainbow vent site (36°14'N, MAR). *Chemical Geology* 216, 329–352.  
792 <https://doi.org/10.1016/j.chemgeo.2004.11.015>
- 793 Chavagnac, V., German, C.R., Taylor, R.N., 2008. Global environmental effects of large volcanic  
794 eruptions on ocean chemistry: Evidence from “hydrothermal” sediments (ODP Leg 185, Site  
795 1149B). *J. Geophys. Res.* 113, B06201. <https://doi.org/10.1029/2007JB005333>
- 796 Cronan, D.S., 1972. The Mid-Atlantic Ridge near 45 °N, XVII: Al, As, Hg, and Mn in Ferruginous  
797 Sediments from the Median Valley. *Can. J. Earth Sci.* 9, 319–323.  
798 <https://doi.org/10.1139/e72-025>
- 799 Deuser, W.G., 1987. Seasonal variations in isotopic composition and deep-water fluxes of the tests of  
800 perennially abundant planktonic foraminifera of the Sargasso Sea; results from sediment-trap  
801 collections and their paleoceanographic significance. *The Journal of Foraminiferal Research*  
802 17, 14–27. <https://doi.org/10.2113/gsjfr.17.1.14>
- 803 Deuser, W.G., Ross, E.H., 1980. Seasonal change in the flux of organic carbon to the deep Sargasso  
804 Sea. *Nature* 283, 364–365. <https://doi.org/10.1038/283364a0>
- 805 Dick, G.J., Anantharaman, K., Baker, B.J., Li, M., Reed, D.C., Sheik, C.S., 2013. The microbiology  
806 of deep-sea hydrothermal vent plumes: ecological and biogeographic linkages to seafloor and  
807 water column habitats. *Front. Microbiol.* 4. <https://doi.org/10.3389/fmicb.2013.00124>
- 808 Ducklow, H., Steinberg, D., Buesseler, K., 2001. Upper Ocean Carbon Export and the Biological  
809 Pump. *oceanog* 14, 50–58. <https://doi.org/10.5670/oceanog.2001.06>
- 810 Dutkiewicz, A., Müller, R.D., Hogg, A.McC., Spence, P., 2016. Vigorous deep-sea currents cause  
811 global anomaly in sediment accumulation in the Southern Ocean. *Geology* 44, 663–666.  
812 <https://doi.org/10.1130/G38143.1>
- 813 Dymond, J., 1981. Geochemistry of Nazca plate surface sediments: An evaluation of hydrothermal,  
814 biogenic, detrital, and hydrogenous sources, in: *Geological Society of America Memoirs*.  
815 Geological Society of America, pp. 133–174. <https://doi.org/10.1130/MEM154-p133>
- 816 Edmonds, H.N., German, C.R., 2004. Particle geochemistry in the Rainbow hydrothermal plume,  
817 Mid-Atlantic Ridge. *Geochimica et Cosmochimica Acta* 68, 759–772.  
818 [https://doi.org/10.1016/S0016-7037\(03\)00498-8](https://doi.org/10.1016/S0016-7037(03)00498-8)
- 819 Emerson, S., Hedges, J.I., 1988. Processes controlling the organic carbon content of open ocean  
820 sediments. *Paleoceanography* 3, 621–634. <https://doi.org/10.1029/PA003i005p00621>
- 821 Escrig, S., Bézous, A., Langmuir, C.H., Michael, P.J., Arculus, R., 2012. Characterizing the effect of  
822 mantle source, subduction input and melting in the Fonualei Spreading Center, Lau Basin:  
823 Constraints on the origin of the boninitic signature of the back-arc lavas: GEOCHEMICAL

- 824 VARIATION ALONG THE FSC. *Geochem. Geophys. Geosyst.* 13, n/a-n/a.  
825 <https://doi.org/10.1029/2012GC004130>
- 826 Ewart, A., Brothers, R.N., Mateen, A., 1977. An outline of the geology and geochemistry, and the  
827 possible petrogenetic evolution of the volcanic rocks of the Tonga-Kermadec-New Zealand  
828 island arc. *Journal of Volcanology and Geothermal Research* 2, 205–250.  
829 [https://doi.org/10.1016/0377-0273\(77\)90001-4](https://doi.org/10.1016/0377-0273(77)90001-4)
- 830 Feely, R.A., Geiselman, T.L., Baker, E.T., Massoth, G.J., Hammond, S.R., 1990. Distribution and  
831 composition of hydrothermal plume particles from the ASHES Vent Field at Axial Volcano,  
832 Juan de Fuca Ridge. *J. Geophys. Res.* 95, 12855. <https://doi.org/10.1029/JB095iB08p12855>
- 833 Feely, R.A., Lewison, M., Massoth, G.J., Robert-Baldo, G., Lavelle, J.W., Byrne, R.H., Von Damm,  
834 K.L., Curl, H.C., 1987. Composition and dissolution of black smoker particulates from active  
835 vents on the Juan de Fuca Ridge. *J. Geophys. Res.* 92, 11347–11363.  
836 <https://doi.org/10.1029/JB092iB11p11347>
- 837 Fiantis, D., Nelson, M., Shamshuddin, J., Goh, T.B., Van Ranst, E., 2010. Determination of the  
838 geochemical weathering indices and trace elements content of new volcanic ash deposits from  
839 Mt. Talang (West Sumatra) Indonesia. *Eurasian Soil Sc.* 43, 1477–1485.  
840 <https://doi.org/10.1134/S1064229310130077>
- 841 Gardner, W., 1980. Field calibration of sediment traps. *Journal of Marine Research* 30, 311–323.
- 842 GEBCO Bathymetric Compilation Group 2022, 2022. The GEBCO\_2022 Grid - a continuous terrain  
843 model of the global oceans and land. [https://doi.org/10.5285/E0F0BB80-AB44-2739-E053-  
844 6C86ABC0289C](https://doi.org/10.5285/E0F0BB80-AB44-2739-E053-6C86ABC0289C)
- 845 German, C.R., Bourlés, D.L., Brown, E.T., Hergt, J., Colley, S., Higgs, N.C., Ludford, E.M., Nelsen,  
846 T.A., Feely, R.A., Raisbeck, G., Yiou, F., 1997. Hydrothermal scavenging on the Juan de  
847 Fuca Ridge: <sup>230</sup>Thxs, <sup>10</sup>Be, and REEs in ridge-flank sediments. *Geochimica et*  
848 *Cosmochimica Acta* 61, 4067–4078. [https://doi.org/10.1016/S0016-7037\(97\)00230-5](https://doi.org/10.1016/S0016-7037(97)00230-5)
- 849 Gersonde, R., Crosta, X., Abelman, A., Armand, L., 2005. Sea-surface temperature and sea ice  
850 distribution of the Southern Ocean at the EPILOG Last Glacial Maximum—a circum-  
851 Antarctic view based on siliceous microfossil records. *Quaternary Science Reviews* 24, 869–  
852 896. <https://doi.org/10.1016/j.quascirev.2004.07.015>
- 853 González-Vega, A., Fraile-Nuez, E., Santana-Casiano, J.M., González-Dávila, M., Escánez-Pérez, J.,  
854 Gómez-Ballesteros, M., Tello, O., Arrieta, J.M., 2020. Significant Release of Dissolved  
855 Inorganic Nutrients From the Shallow Submarine Volcano Tagoro (Canary Islands) Based on  
856 Seven-Year Monitoring. *Front. Mar. Sci.* 6, 829. <https://doi.org/10.3389/fmars.2019.00829>
- 857 Guieu, C., 2020. TONGA RECUP cruise, Alis R/V. <https://doi.org/10.17600/18001357>
- 858 Guieu, C., Bonnet, S., 2019. TONGA cruise 2019, L'Atalante R/V.  
859 <https://doi.org/10.17600/18000884>
- 860 Guieu, C., Bonnet, S., Abadou, F., Alliouane, S., Arnaud-Haond, S., Arnone, V., Baudoux, A.-C.,  
861 Baumas, C., Beillard, L., Benavides, M., Berman-Frank, I., Bhairy, N., Bigeard, E., Boulart,  
862 C., Bouruet-Aubertot, P., Boyd, P., Bressac, M., Camps, M., Chaffron, S., Chavagnac, V.,  
863 Chevaillier, S., Collot, J., Cuypers, Y., De Liège, G., De Saint Léger, E., De Vargas, C.,  
864 Desboeufs, K., Desgranges, M.-M., Destrigneville, C., Dimier, C., Diruit, W., Dissard, D.,  
865 Doussin, J.-F., Dufour, A., Dulaquais, G., Fernandez, J.-M., Feron, A., Ferrieux, M., Filella,  
866 A., Forrer, H., Fourrier, P., Gac, J.-P., Gachenot, M., Gaimoz, C., Garczarek, L., Gazeau, F.,

- 867 Gonzalez, A., Gonzalez Santana, D., Gorgues, T., Grima, N., Grisoni, J.-M., Grosso, O.,  
868 Guigue, C., Habasque, J., Heimbürger-Boavida, L.-E., Jeandel, C., Jeanthon, C., Journet, E.,  
869 Knapp, A., Lacan, F., Le Gall, F., Le Moal, P., Le Moigne, F., Leblanc, K., Leblond, N.,  
870 Lebourges-Dhaussy, A., Leconte, J., Lefèvre, D., Lombard, F., Lorrain, A., Lory, C., Maes,  
871 C., Mahieu, L., Marie, D., Mazoyer, C., Menkes, C., Michoud, V., Montanes, M., Not, F.,  
872 Nunige, S., Paparella, F., Patriat, M., Pelletier, B., Petrenko, A., Planquette, H., Point, D.,  
873 Portlock, G., Probert, I., Pulido-Villena, E., Ratin, M., Ratnarajah, L., Riso, R., Rizzo, A.,  
874 Salaun, P., Sarthou, G., Schmechtig, C., Sellegri, K., Simon, N., Tagliabue, A., Taillandier,  
875 V., Tamburini, C., Tedetti, M., Thibon, F., Tilliette, C., Torres Rodriguez, N., Triquet, S.,  
876 Uitz, J., Van Wambeke, F., Vaulot, D., Vigier, N., Vilain, M., Vorrath, M.H., Weppe, L.,  
877 Whitby, H., 2022. Biogeochemical dataset collected during the TONGA cruise.  
878 <https://doi.org/10.17882/88169>
- 879 Guieu, C., Bonnet, S., Petrenko, A., Menkes, C., Chavagnac, V., Desboeufs, K., Maes, C., Moutin,  
880 T., 2018. Iron from a submarine source impacts the productive layer of the Western Tropical  
881 South Pacific (WTSP). *Sci Rep* 8, 1–9. <https://doi.org/10.1038/s41598-018-27407-z>
- 882 Guieu, C., Roy-Barman, M., Leblond, N., Jeandel, C., Souhaut, M., Le Cann, B., Dufour, A.,  
883 Bournot, C., 2005. Vertical particle flux in the northeast Atlantic Ocean (POMME  
884 experiment). *Journal of Geophysical Research: Oceans* 110.  
885 <https://doi.org/10.1029/2004JC002672>
- 886 Hargrave, B.T., Burns, N.M., 1979. Assessment of sediment trap collection efficiency. *Limnol.*  
887 *Oceanogr.* 24, 1124–1136. <https://doi.org/10.4319/lo.1979.24.6.1124>
- 888 Ho, T.-Y., Quigg, A., Finkel, Z.V., Milligan, A.J., Wyman, K., Falkowski, P.G., Morel, F.M.M.,  
889 2003. The Elemental Composition of Some Marine Phytoplankton. *Journal of Phycology* 39,  
890 1145–1159. <https://doi.org/10.1111/j.0022-3646.2003.03-090.x>
- 891 Honjo, S., Spencer, D.W., Gardner, W.D., 1992. A sediment trap intercomparison experiment in the  
892 Panama Basin, 1979. *Deep Sea Research Part A. Oceanographic Research Papers* 39, 333–  
893 358. [https://doi.org/10.1016/0198-0149\(92\)90112-7](https://doi.org/10.1016/0198-0149(92)90112-7)
- 894 Horn, D.R., Horn, B.M., Delach, M.N., 1970. Sedimentary Provinces of the North Pacific, in:  
895 *Geological Society of America Memoirs*. Geological Society of America, pp. 1–22.  
896 <https://doi.org/10.1130/MEM126-p1>
- 897 Humphris, S.E., Herzig, P.M., Miller, D.J., Alt, J.C., Becker, K., Brown, D., Brüggemann, G., Chiba,  
898 H., Fouquet, Y., Gemmell, J.B., Guerin, G., Hannington, M.D., Holm, N.G., Honnorez, J.J.,  
899 Iturrino, G.J., Knott, R., Ludwig, R., Nakamura, K., Petersen, S., Reysenbach, A.-L., Rona,  
900 P.A., Smith, S., Sturz, A.A., Tivey, M.K., Zhao, X., 1995. The internal structure of an active  
901 sea-floor massive sulphide deposit. *Nature* 377, 713–716. <https://doi.org/10.1038/377713a0>
- 902 Hüneke, H., Henrich, R., 2011. Pelagic Sedimentation in Modern and Ancient Oceans, in:  
903 *Developments in Sedimentology*. Elsevier, pp. 215–351. [https://doi.org/10.1016/B978-0-444-](https://doi.org/10.1016/B978-0-444-53000-4.00004-4)  
904 [53000-4.00004-4](https://doi.org/10.1016/B978-0-444-53000-4.00004-4)
- 905 Hurd, D.C., 1972. Factors affecting solution rate of biogenic opal in seawater. *Earth and Planetary*  
906 *Science Letters* 15, 411–417. [https://doi.org/10.1016/0012-821X\(72\)90040-4](https://doi.org/10.1016/0012-821X(72)90040-4)
- 907 Imai, N., Terashima, S., Itoh, S., Ando, A., 1995. 1994 Compilation of analytical data for minor and  
908 trace elements in seventeen GSJ geochemical reference samples, “igneous rock series.”  
909 *Geostandards and Geoanalytical Research* 19, 135–213. [https://doi.org/10.1111/j.1751-](https://doi.org/10.1111/j.1751-908X.1995.tb00158.x)  
910 [908X.1995.tb00158.x](https://doi.org/10.1111/j.1751-908X.1995.tb00158.x)

- 911 Johnson, K.S., Gordon, R.M., Coale, K.H., 1997. What controls dissolved iron concentrations in the  
912 world ocean? *Marine Chemistry* 57, 137–161. [https://doi.org/10.1016/S0304-4203\(97\)00043-](https://doi.org/10.1016/S0304-4203(97)00043-1)  
913 1
- 914 Karl, D.M., 1995. *The microbiology of deep-sea hydrothermal vents*, CRC-Press. ed.
- 915 Kipp, L.E., Sanial, V., Henderson, P.B., van Beek, P., Reyss, J.-L., Hammond, D.E., Moore, W.S.,  
916 Charette, M.A., 2018. Radium isotopes as tracers of hydrothermal inputs and neutrally  
917 buoyant plume dynamics in the deep ocean. *Marine Chemistry* 201, 51–65.  
918 <https://doi.org/10.1016/j.marchem.2017.06.011>
- 919 Klaas, C., Archer, D.E., 2002. Association of sinking organic matter with various types of mineral  
920 ballast in the deep sea: Implications for the rain ratio. *Global Biogeochem. Cycles* 16, 63-1-  
921 63–14. <https://doi.org/10.1029/2001GB001765>
- 922 Kyte, F.T., Leinen, M., Ross Heath, G., Zhou, L., 1993. Cenozoic sedimentation history of the  
923 central North Pacific: Inferences from the elemental geochemistry of core LL44-GPC3.  
924 *Geochimica et Cosmochimica Acta* 57, 1719–1740. [https://doi.org/10.1016/0016-](https://doi.org/10.1016/0016-7037(93)90109-A)  
925 7037(93)90109-A
- 926 Leinen, M., 1989. The pelagic clay province of the North Pacific Ocean, in: Winterer, E.L., Hussong,  
927 D.M., Decker, R.W. (Eds.), *The Eastern Pacific Ocean and Hawaii*. Geological Society of  
928 America, North America, pp. 323–335. <https://doi.org/10.1130/DNAG-GNA-N.323>
- 929 Leonelli, C., Kamseu, E., Boccaccini, D.N., Melo, U.C., Rizzuti, A., Billong, N., Miselli, P., 2007.  
930 Volcanic ash as alternative raw materials for traditional vitrified ceramic products. *Advances*  
931 *in Applied Ceramics* 106, 135–141. <https://doi.org/10.1179/174367607X159329>
- 932 Li, Y.-H., Schoonmaker, J.E., 2003. Chemical Composition and Mineralogy of Marine Sediments, in:  
933 *Treatise on Geochemistry*. Elsevier, pp. 1–35. [https://doi.org/10.1016/B0-08-043751-](https://doi.org/10.1016/B0-08-043751-6/07088-2)  
934 6/07088-2
- 935 Lilley, M.D., Feely, R.A., Trefry, J.H., 2013. Chemical and Biochemical Transformations in  
936 Hydrothermal Plumes, in: *Seafloor Hydrothermal Systems: Physical, Chemical, Biological,*  
937 *and Geological Interactions*. American Geophysical Union (AGU), pp. 369–391.  
938 <https://doi.org/10.1029/GM091p0369>
- 939 Locarnini, R., Mishonov, A., Baranova, O., Boyer, T., Zweng, M., Garcia, H., Reagan, J., Seidov, D.,  
940 Weathers, K., Paver, C., 2018. *World Ocean Atlas 2018, Volume 1: Temperature*. NOAA  
941 Atlas NESDIS 81 52.
- 942 Lou, Y., He, Z., Han, X., 2020. Transport and Deposition Patterns of Particles Laden by Rising  
943 Submarine Hydrothermal Plumes. *Geophys. Res. Lett.* 47.  
944 <https://doi.org/10.1029/2020GL089935>
- 945 Lupton, J.E., Pyle, D.G., Jenkins, W.J., Greene, R., Evans, L., 2004. Evidence for an extensive  
946 hydrothermal plume in the Tonga-Fiji region of the South Pacific. *Geochem. Geophys.*  
947 *Geosyst.* 5. <https://doi.org/10.1029/2003GC000607>
- 948 Mahiques, M.M., Sousa, S.H.M., Burone, L., Nagai, R.H., Silveira, I.C.A., Figueira, R.C.L.,  
949 Soutelino, R.G., Ponsoni, L., Klein, D.A., 2011. Radiocarbon geochronology of the sediments  
950 of the São Paulo Bight (southern Brazilian upper margin). *An. Acad. Bras. Ciênc.* 83, 817–  
951 834. <https://doi.org/10.1590/S0001-37652011005000028>
- 952 Massoth, G., Baker, E., Worthington, T., Lupton, J., de Ronde, C., Arculus, R., Walker, S.,  
953 Nakamura, K., Ishibashi, J., Stoffers, P., Resing, J., Greene, R., Lebon, G., 2007. Multiple

- 954 hydrothermal sources along the south Tonga arc and Valu Fa Ridge. *Geochem. Geophys.*  
955 *Geosyst.* 8. <https://doi.org/10.1029/2007GC001675>
- 956 Massoth, G.J., Baker, E.T., Feely, R.A., Lupton, J.E., Collier, R.W., Gendron, J.F., Roe, K.K.,  
957 Maenner, S.M., Resing, J.A., 1998. Manganese and iron in hydrothermal plumes resulting  
958 from the 1996 Gorda Ridge Event. *Deep Sea Research Part II: Topical Studies in*  
959 *Oceanography* 45, 2683–2712. [https://doi.org/10.1016/S0967-0645\(98\)00089-7](https://doi.org/10.1016/S0967-0645(98)00089-7)
- 960 McCave, I.N., 1975. Vertical flux of particles in the ocean. *Deep Sea Research and Oceanographic*  
961 *Abstracts* 22, 491–502. [https://doi.org/10.1016/0011-7471\(75\)90022-4](https://doi.org/10.1016/0011-7471(75)90022-4)
- 962 Mills, R., Elderfield, H., Thomson, J., 1993. A dual origin for the hydrothermal component in a  
963 metalliferous sediment core from the Mid-Atlantic Ridge. *J. Geophys. Res.* 98, 9671.  
964 <https://doi.org/10.1029/92JB01414>
- 965 Mills, R.A., Elderfield, H., 1995. Hydrothermal Activity and the Geochemistry of Metalliferous  
966 Sediment, in: Humphris, S.E., Zierenberg, R.A., Mullineaux, L.S., Thomson, R.E. (Eds.),  
967 *Geophysical Monograph Series*. American Geophysical Union, Washington, D. C., pp. 392–  
968 407. <https://doi.org/10.1029/GM091p0392>
- 969 Morse, J.W., Arvidson, R.S., Lüttge, A., 2007. Calcium Carbonate Formation and Dissolution.  
970 *Chem. Rev.* 107, 342–381. <https://doi.org/10.1021/cr050358j>
- 971 Mortlock, R.A., Froelich, P.N., 1989. A simple method for the rapid determination of biogenic opal  
972 in pelagic marine sediments. *Deep Sea Research Part A. Oceanographic Research Papers* 36,  
973 1415–1426. [https://doi.org/10.1016/0198-0149\(89\)90092-7](https://doi.org/10.1016/0198-0149(89)90092-7)
- 974 Mosseri, J., Quéguiner, B., Rimmelin, P., Leblond, N., Guieu, C., 2005. Silica fluxes in the northeast  
975 Atlantic frontal zone of Mode Water formation (38°–45°N, 16°–22°W) in 2001–2002. *J.*  
976 *Geophys. Res.* 110, C07S19. <https://doi.org/10.1029/2004JC002615>
- 977 Naji, J.A., Asi, I.M., 2008. Performance Evaluation of Asphalt Concrete Mixes Containing Granular  
978 Volcanic Ash. *J. Mater. Civ. Eng.* 20, 754–761. [https://doi.org/10.1061/\(ASCE\)0899-1561\(2008\)20:12\(754\)](https://doi.org/10.1061/(ASCE)0899-1561(2008)20:12(754))
- 980 Nelson, D.M., Brzezinski, M.A., 1997. Diatom growth and productivity in an oligo-trophic midocean  
981 gyre: A 3-yr record from the Sargasso Sea near Bermuda. *Limnol. Oceanogr.* 42, 473–486.  
982 <https://doi.org/10.4319/lo.1997.42.3.0473>
- 983 Nelson, D.M., Smith, W.O., Muench, R.D., Gordon, L.I., Sullivan, C.W., Husby, D.M., 1989.  
984 Particulate matter and nutrient distributions in the ice-edge zone of the Weddell Sea:  
985 relationship to hydrography during late summer. *Deep Sea Research Part A. Oceanographic*  
986 *Research Papers* 36, 191–209. [https://doi.org/10.1016/0198-0149\(89\)90133-7](https://doi.org/10.1016/0198-0149(89)90133-7)
- 987 Nelson, D.M., Tréguer, P., Brzezinski, M.A., Leynaert, A., Quéguiner, B., 1995. Production and  
988 dissolution of biogenic silica in the ocean: Revised global estimates, comparison with  
989 regional data and relationship to biogenic sedimentation. *Global Biogeochemical Cycles* 9,  
990 359–372. <https://doi.org/10.1029/95GB01070>
- 991 Ng, W.-L., Chen, C.-A., Kawi, S.D., Musta, B., Chan, T.-Y., 2019. Effects of hydrogen peroxide  
992 treatment on the particle size distribution of hydrothermal vent sediments: A case study in  
993 Guishan Island, Taiwan. *Borneo Journal of Marine Science and Aquaculture (BJoMSA)* 3,  
994 52–56. <https://doi.org/10.51200/bjomsa.v3i2.1995>

- 995 Nohara, M., Yokoto, S., 1978. The Geochemistry of Trace Elements in Pelagic Sediments from the  
 996 Central Pacific Basin. *The Journal of the Geological Society of Japan* 84.  
 997 <https://doi.org/10.5575/geosoc.84.165>
- 998 Oskarasson, N., 2010. Chemical analysis of rocks from the Eyjafjallajökull 2010 eruptions.
- 999 Pelletier, B., Calmant, S., Pillet, R., 1998. Current tectonics of the Tonga–New Hebrides region.  
 1000 *Earth and Planetary Science Letters* 164, 263–276. [https://doi.org/10.1016/S0012-](https://doi.org/10.1016/S0012-821X(98)00212-X)  
 1001 [821X\(98\)00212-X](https://doi.org/10.1016/S0012-821X(98)00212-X)
- 1002 Piper, D.J.W., 2005. SEDIMENTARY PROCESSES | Deep Water Processes and Deposits, in:  
 1003 *Encyclopedia of Geology*. Elsevier, pp. 641–649. [https://doi.org/10.1016/B0-12-369396-](https://doi.org/10.1016/B0-12-369396-9/00496-2)  
 1004 [9/00496-2](https://doi.org/10.1016/B0-12-369396-9/00496-2)
- 1005 Plank, S., Marchese, F., Genzano, N., Nolde, M., Martinis, S., 2020. The short life of the volcanic  
 1006 island New Late’iki (Tonga) analyzed by multi-sensor remote sensing data. *Sci Rep* 10,  
 1007 22293. <https://doi.org/10.1038/s41598-020-79261-7>
- 1008 Plank, T., Kelley, K.A., Murray, R.W., Stern, L.Q., 2007. Chemical composition of sediments  
 1009 subducting at the Izu-Bonin trench: CHEMICAL COMPOSITION OF SEDIMENTS.  
 1010 *Geochem. Geophys. Geosyst.* 8, n/a-n/a. <https://doi.org/10.1029/2006GC001444>
- 1011 Raven, J.A., 1988. The iron and molybdenum use efficiencies of plant growth with different energy,  
 1012 carbon and nitrogen sources. *New Phytol* 109, 279–287. [https://doi.org/10.1111/j.1469-](https://doi.org/10.1111/j.1469-8137.1988.tb04196.x)  
 1013 [8137.1988.tb04196.x](https://doi.org/10.1111/j.1469-8137.1988.tb04196.x)
- 1014 Razzhigaeva, N.G., Ganzei, L.A., Grebennikova, T.A., Mokhova, L.M., Kopoteva, T.A., Rybin,  
 1015 A.V., Kharlamov, A.A., 2009. The peat bog of Ketoi Island: The Middle-Upper Holocene  
 1016 reference section of the Central Kuriles. *Russ. J. of Pac. Geol.* 3, 570–584.  
 1017 <https://doi.org/10.1134/S1819714009060050>
- 1018 Redfield, A.C., Ketchum, B.H., Richards, F.A., 1963. The influence of organisms on the composition  
 1019 of sea-water, in: *The Composition of Seawater: Comparative and Descriptive Oceanography*,  
 1020 *The Sea*. Interscience Publishers: New York, pp. 26–77.
- 1021 Resing, J.A., Sansone, F.J., 1999. The chemistry of lava–seawater interactions: the generation of  
 1022 acidity. *Geochimica et Cosmochimica Acta* 63, 2183–2198. [https://doi.org/10.1016/S0016-](https://doi.org/10.1016/S0016-7037(99)00193-3)  
 1023 [7037\(99\)00193-3](https://doi.org/10.1016/S0016-7037(99)00193-3)
- 1024 Resing, J.A., Sedwick, P.N., German, C.R., Jenkins, W.J., Moffett, J.W., Sohst, B.M., Tagliabue, A.,  
 1025 2015. Basin-scale transport of hydrothermal dissolved metals across the South Pacific Ocean.  
 1026 *Nature* 523, 200–203. <https://doi.org/10.1038/nature14577>
- 1027 Robbins, J.A., Edgington, D.N., 1975. Determination of recent sedimentation rates in Lake Michigan  
 1028 using Pb-210 and Cs-137. *Geochimica et Cosmochimica Acta* 39, 285–304.  
 1029 [https://doi.org/10.1016/0016-7037\(75\)90198-2](https://doi.org/10.1016/0016-7037(75)90198-2)
- 1030 Rousselet, L., de Verneil, A., Doglioli, A.M., Petrenko, A.A., Duhamel, S., Maes, C., Blanke, B.,  
 1031 2018. Large- to submesoscale surface circulation and its implications on  
 1032 biogeochemical/biological horizontal distributions during the OUTPACE cruise (southwest  
 1033 Pacific). *Biogeosciences* 15, 2411–2431. <https://doi.org/10.5194/bg-15-2411-2018>
- 1034 Sakaguchi, A., Kimura, G., Strasser, M., Sreaton, E.J., Curewitz, D., Murayama, M., 2011. Episodic  
 1035 seafloor mud brecciation due to great subduction zone earthquakes. *Geology* 39, 919–922.  
 1036 <https://doi.org/10.1130/G32043.1>

- 1037 Sarmiento, J.L., Gruber, N., 2006. Ocean biogeochemical dynamics. Princeton University Press,  
1038 Princeton.
- 1039 Sayles, F.L., Bischoff, J.L., 1973. Ferromanganous sediments in the equatorial East Pacific. *Earth  
1040 and Planetary Science Letters* 19, 330–336. [https://doi.org/10.1016/0012-821X\(73\)90083-6](https://doi.org/10.1016/0012-821X(73)90083-6)
- 1041 Schmidt, S., Howa, H., Diallo, A., Martín, J., Cremer, M., Duros, P., Fontanier, C., Deflandre, B.,  
1042 Metzger, E., Mulder, T., 2014. Recent sediment transport and deposition in the Cap-Ferret  
1043 Canyon, South-East margin of Bay of Biscay. *Deep Sea Research Part II: Topical Studies in  
1044 Oceanography* 104, 134–144. <https://doi.org/10.1016/j.dsr2.2013.06.004>
- 1045 Stoffers, P., Worthington, T.J., Schwarz-Schampera, U., Hannington, M.D., Massoth, G.J., Hekinian,  
1046 R., Schmidt, M., Lundsten, L.J., Evans, L.J., Vaiomo'unga, R., Kerby, T., 2006. Submarine  
1047 volcanoes and high-temperature hydrothermal venting on the Tonga arc, southwest Pacific.  
1048 *Geol* 34, 453. <https://doi.org/10.1130/G22227.1>
- 1049 Taylor, S.R., 1964. Abundance of chemical elements in the continental crust: a new table.  
1050 *Geochimica et Cosmochimica Acta* 28, 1273–1285. [https://doi.org/10.1016/0016-  
1051 7037\(64\)90129-2](https://doi.org/10.1016/0016-7037(64)90129-2)
- 1052 Taylor, S.R., McLennan, S.M., 1985. The continental crust: its composition and evolution: an  
1053 examination of the geochem. record preserved in sedimentary rocks, *Geoscience texts*.  
1054 Blackwell, Oxford.
- 1055 Tchakoute Kouamo, H., Elimbi, A., Mbey, J.A., Ngally Sabouang, C.J., Njopwouo, D., 2012. The  
1056 effect of adding alumina-oxide to metakaolin and volcanic ash on geopolymer products: A  
1057 comparative study. *Construction and Building Materials* 35, 960–969.  
1058 <https://doi.org/10.1016/j.conbuildmat.2012.04.023>
- 1059 Tilliette, C., Gazeau, F., Portlock, G., Benavides, M., Bonnet, S., Guigue, C., Leblond, N., Lory, C.,  
1060 Marie, D., Montanes, M., Pulido-Villena, E., Sarthou, G., Tedetti, M., Vorrath, M.-E.,  
1061 Whitby, H., Guieu, C., 2023. Influence of shallow hydrothermal fluid release on the  
1062 functioning of phytoplankton communities. *Front. Mar. Sci.* 10, 1082077.  
1063 <https://doi.org/10.3389/fmars.2023.1082077>
- 1064 Tilliette, C., Taillandier, V., Bouruet-Aubertot, P., Grima, N., Maes, C., Montanes, M., Sarthou, G.,  
1065 Vorrath, M.-E., Arnone, V., Bressac, M., González-Santana, D., Gazeau, F., Guieu, C., 2022.  
1066 Dissolved iron patterns impacted by shallow hydrothermal sources along a transect through  
1067 the Tonga-Kermadec arc. *Global Biogeochemical Cycles*.  
1068 <https://doi.org/10.1029/2022GB007363>
- 1069 Timm, C., Bassett, D., Graham, I.J., Leybourne, M.I., de Ronde, C.E.J., Woodhead, J., Layton-  
1070 Matthews, D., Watts, A.B., 2013. Louisville seamount subduction and its implication on  
1071 mantle flow beneath the central Tonga–Kermadec arc. *Nat Commun* 4, 1720.  
1072 <https://doi.org/10.1038/ncomms2702>
- 1073 Tréguer, P., Nelson, D.M., Van Bennekom, A.J., DeMaster, D.J., Leynaert, A., Quéguiner, B., 1995.  
1074 The Silica Balance in the World Ocean: A Reestimate. *Science* 268, 375–379.  
1075 <https://doi.org/10.1126/science.268.5209.375>
- 1076 Trocine, R.P., Trefry, J.H., 1988. Distribution and chemistry of suspended particles from an active  
1077 hydrothermal vent site on the Mid-Atlantic Ridge at 26°N. *Earth and Planetary Science  
1078 Letters* 88, 1–15. [https://doi.org/10.1016/0012-821X\(88\)90041-6](https://doi.org/10.1016/0012-821X(88)90041-6)

- 1079 Turner, J., 2002. Zooplankton fecal pellets, marine snow and sinking phytoplankton blooms. *Aquat.*  
1080 *Microb. Ecol.* 27, 57–102. <https://doi.org/10.3354/ame027057>
- 1081 Verardo, D.J., Froelich, P.N., McIntyre, A., 1990. Determination of organic carbon and nitrogen in  
1082 marine sediments using the Carlo Erba NA-1500 analyzer. *Deep Sea Research Part A.*  
1083 *Oceanographic Research Papers* 37, 157–165. [https://doi.org/10.1016/0198-0149\(90\)90034-S](https://doi.org/10.1016/0198-0149(90)90034-S)
- 1084 Volk, T., Hoffert, M.I., 2013. Ocean Carbon Pumps: Analysis of Relative Strengths and Efficiencies  
1085 in Ocean-Driven Atmospheric CO<sub>2</sub> Changes, in: Sundquist, E.T., Broecker, W.S. (Eds.),  
1086 *Geophysical Monograph Series*. American Geophysical Union, Washington, D. C., pp. 99–  
1087 110. <https://doi.org/10.1029/GM032p0099>
- 1088 Von Damm, K.L., 1990. Seafloor hydrothermal activity: black smoker chemistry and chimneys.  
1089 *Annual Review of Earth and Planetary Sciences* 18, 173–204.
- 1090 Wefer, G., Fischer, G., 1993. Seasonal patterns of vertical particle flux in equatorial and coastal  
1091 upwelling areas of the eastern Atlantic. *Deep Sea Research Part I: Oceanographic Research*  
1092 *Papers* 40, 1613–1645. [https://doi.org/10.1016/0967-0637\(93\)90019-Y](https://doi.org/10.1016/0967-0637(93)90019-Y)
- 1093 Whiteside, A., Dupouy, C., Singh, A., Bani, P., Tan, J., Frouin, R., 2023. Impact of ashes from the  
1094 2022 Tonga volcanic eruption on satellite ocean color signatures. *Front. Mar. Sci.* 9, 1028022.  
1095 <https://doi.org/10.3389/fmars.2022.1028022>
- 1096 Whiteside, A., Dupouy, C., Singh, A., Frouin, R., Menkes, C., Lefèvre, J., 2021. Automatic  
1097 Detection of Optical Signatures within and around Floating Tonga-Fiji Pumice Rafts Using  
1098 MODIS, VIIRS, and OLCI Satellite Sensors. *Remote Sensing* 13, 501.  
1099 <https://doi.org/10.3390/rs13030501>
- 1100 Zhang, H., Che, H., Xia, J., Cheng, Q., Qi, D., Cao, J., Luo, Y., 2022. Sedimentary CaCO<sub>3</sub>  
1101 Accumulation in the Deep West Pacific Ocean. *Front. Earth Sci.* 10, 857260.  
1102 <https://doi.org/10.3389/feart.2022.857260>
- 1103 Zhang, Q., Snow, J.T., Holdship, P., Price, D., Watson, P., Rickaby, R.E.M., 2018. Direct  
1104 measurement of multi-elements in high matrix samples with a flow injection ICP-MS:  
1105 application to the extended *Emiliana huxleyi* Redfield ratio. *J. Anal. At. Spectrom.* 33, 1196–  
1106 1208. <https://doi.org/10.1039/C8JA00031J>
- 1107 Zierenberg, R.A., Adams, M.W.W., Arp, A.J., 2000. Life in extreme environments: Hydrothermal  
1108 vents. *Proceedings of the National Academy of Sciences* 97, 12961–12962.  
1109 <https://doi.org/10.1073/pnas.210395997>
- 1110 Ziveri, P., Rutten, A., de Lange, G.J., Thomson, J., Corselli, C., 2000. Present-day coccolith fluxes  
1111 recorded in central eastern Mediterranean sediment traps and surface sediments.  
1112 *Palaeogeography, Palaeoclimatology, Palaeoecology* 158, 175–195.  
1113 [https://doi.org/10.1016/S0031-0182\(00\)00049-3](https://doi.org/10.1016/S0031-0182(00)00049-3)  
1114